

Linking neuronal avalanches with oscillatory and broadband $1/f$ activities in the resting human brain

Damián Dellavale^{a,*}, Giovanni Rabuffo^{b,1}, Emahnuel Troisi Lopez^c, Antonella Romano^d, Pierpaolo Sorrentino^{b,e,f,1,*}

^a*Consejo Nacional de Investigaciones Científicas y Técnicas (CONICET), Centro Atómico Bariloche, R8402AGP, San Carlos de Bariloche, Río Negro, Argentina.*

^b*Institut de Neurosciences des Systèmes, Aix-Marseille Université, Marseille, France.*

^c*Institute of Applied Sciences and Intelligent Systems, National Research Council (CNR), 80078, Pozzuoli, Italy.*

^d*University of Naples Parthenope, Department of Motor Science and Wellness, Naples, Italy.*

^e*Department of Biomedical Science, University of Sassari, Sassari, Italy.*

^f*Institute of Applied Sciences and Intelligent Systems, National Research Council (CNR), Naples, Italy.*

Abstract

Objective:

Brain oscillations, broadband $1/f$ activity and neuronal avalanches (NA) are valuable conceptualizations extensively used to interpret brain data, yet, these perspectives have mainly progressed in parallel with no current consensus on a rationale linking them. This study aims to reconcile these viewpoints using source-reconstructed MEG data obtained in healthy humans during eyes-closed resting state.

Methods:

We analyzed NA in source-reconstructed MEG data from 47 subjects. For this, we introduced custom measures and a comprehensive array of features characterizing the statistical, spatiotemporal and spectral properties of NA. By using the complex baseband representation of signals we provide an analytical description of the mechanisms underlying the emergence of NA from the Fourier spectral constituents of the brain activity.

Results:

The observed NA disclose a significant spectral signature in the alpha band, suggesting that the large-scale spreading of alpha bursts occurs mainly via brain avalanches. Besides, the NA detected in our MEG dataset can be segregated based on their spectral signature in two main groups having different propagation patterns, where cluster 2 avalanches is mainly related to the spread of

*Corresponding authors.

Email addresses: dellavale@cab.cnea.gov.ar (Damián Dellavale), pierpaolo.sorrentino@univ-amu.fr (Pierpaolo Sorrentino)

¹Co-last authors.

narrowband alpha bursts across the brain network, whereas cluster 1 avalanches correspond to more spatially localized fluctuations promoted by the broadband $1/f$ activity. We also provide an analytical framework for the evidence showing that a) spectral group delay consistency in specific narrow frequency bands, b) transient cross-regional coherent oscillations and c) broadband $1/f$ activity, are all key ingredients for the emergence of realistic avalanches.

Significance:

The proposed analytical arguments, supported by extensive model and experimental evidence, show how NA emerge from narrowband oscillations and broadband arrhythmic activity co-existing in the human brain. Our results suggest that large-scale spreading of specific narrowband oscillations takes place in a transient manner mainly via NA, which may play a functional role as a long-range interaction mechanism in the resting human brain.

Keywords: human MEG, neuronal avalanches, brain oscillations, broadband $1/f$ activity, group delay, complex baseband representation

1 Highlights

- 2 • Neuronal avalanches propagating across the brain during spontaneous rest-

3 ing state activity, are highly structured in terms of their spatial, temporal

4 and spectral properties.
- 5 • The link between local above-threshold fluctuations and oscillations can

6 be understood in terms of the group delay consistency across the spectral

7 components of the neuronal activity (spectral group delay consistency).
- 8 • Spectral group delay consistency, transient cross-regional coherent oscilla-

9 tions and broadband $1/f$ activity, are all key ingredients for the emergence

10 of realistic avalanches.
- 11 • Observed neuronal avalanches can be segregated based on their spectral

12 signature in two main groups having different propagation patterns, where

13 cluster 2 avalanches is specifically related to the spread of narrowband

14 alpha bursts across the brain network, whereas cluster 1 avalanches corre-

15 spond to more spatially localized fluctuations promoted by the broadband

16 $1/f$ activity.
- 17 • Large-scale spreading of alpha bursts occurs mainly via brain avalanches,

18 which may play a functional role as a long-range interaction mechanism

19 in the resting human brain.

20 1. INTRODUCTION

21 The human brain generates complex behaviors from the coordinated in-

22 teraction of neuronal populations, with evidence showing different degrees of

specialization/distribution of these networks. Such coordination is accompanied (or driven) by neural activity patterns that can be measured using techniques like electroencephalography (EEG) or magnetoencephalography (MEG). In general, brain signals are characterized by both narrowband rhythmic (i.e., oscillations) and broadband arrhythmic (i.e., $1/f$ spectral profile) components [1]. Oscillatory neural activity consists of rhythmic (i.e., periodic) fluctuations in the brain's signals, which occur across various narrow frequency bands and have been associated with specific cognitive functions [2]. For example, the alpha rhythm, typically between 8–13 Hz, emerges during closed-eyes wakefulness [3, 4, 5], while the gamma rhythm, exceeding 30 Hz, has been proposed to play a role in higher cognitive processes [6]. These oscillatory components manifest as "bumps" in the signals' Power Spectral Density (PSD). In contrast to brain oscillations, broadband arrhythmic neural activity exhibits a more complex and irregular nature, often associated with scale-free dynamics (i.e., no characteristic temporal scale) [1]. It generally displays a $1/f$ decay pattern in the PSD, featuring a fractal-like distribution of power across frequencies. This broadband noise-like activity contributes significantly to the brain's overall signal and is intricately linked with cognitive processes, potentially carrying valuable information [7]. Traditionally, the study of brain *narrowband oscillations* and *broadband $1/f$ activity* has provided two lenses through which electrophysiological data have been examined [8]. In general, spectral attributes like power and phase offer rich insights into brain dynamics, enabling the discrimination of brain activity during perceptual tasks and distinguishing between healthy and pathological dynamics in resting states [9]. Besides narrowband oscillations and broadband $1/f$ activity, the analysis of collective brain dynamics reveals that system-level neuronal activity is interspersed by *salient network events*. During these events, subsets of brain regions collectively exhibit rare fluctuations above a threshold (e.g., signal amplitude > 3 standard deviations), igniting from specific brain sites, propagating across the brain circuitry in an avalanche-like cascade of activations, and finally decaying below the threshold. For this reason, these salient network events are sometimes referred to as neuronal avalanches. Neuronal avalanches occur aperiodically and are consistently observed across imaging modalities, including multielectrode array recordings [10, 11], EEG [12, 13], MEG [12, 14], SEEG [15, 16], fMRI [17], and calcium imaging [18, 19]. Neuronal avalanches have drawn considerable interest due to their potential significance in information processing [20, 21], facilitating responses with a wide dynamical range [22, 23], and playing a role in achieving flexible dynamics [24, 25, 26]. These events were largely studied in the context of the "critical brain hypothesis", which posits that the brain might be operating near a critical point (i.e., at the edge of a phase transition). In fact, neuronal avalanches display hallmark properties expected in systems that self-organize at a critical point, such as the power-law distribution of avalanche durations (life span) and sizes (number of regions recruited) [12, 14, 27]. For the sake of generality, in this manuscript, we will refer to *salient network events*, or *neuronal avalanches* interchangeably, without implying a connection to the brain criticality hypothesis. While narrowband oscillations, broadband $1/f$ ac-

69 tivity, and neuronal avalanches offer valuable conceptualizations to interpret
70 brain data, these well-established perspectives have mainly progressed in parallel,
71 with only limited literature linking them [28, 29, 30]. Given the ubiquitous
72 and concurrent presence of oscillations, broadband $1/f$ activity, and neuronal
73 avalanches in the brain during rest, a fundamental question arises: Can we es-
74 tablish a connection between these perspectives? In other words, can we invoke
75 a parsimonious explanation that justifies the simultaneous presence of these
76 phenomena? This study aims to reconcile these viewpoints by studying the re-
77 lation between narrowband oscillations, broadband $1/f$ activity, and neuronal
78 avalanches in source-reconstructed MEG data where healthy participants are
79 recorded during eyes-closed resting state. In this condition, the characteristic
80 alpha peak and $1/f$ decay in the PSD are observed in brain signals, concurrently
81 with neuronal avalanches.

82 2. METHODS

83 2.1. Participants and data

84 In this study we analyzed a source-reconstructed MEG dataset previously
85 published in [31, 25]. In short, 58 young adults (32 males/26 females, mean
86 age \pm SD was 30.72 ± 11.58) were recruited from the general community. All
87 participants were right-handed and native Italian speakers. The inclusion cri-
88 teria were (1) no major internal, neurological, or psychiatric illnesses; and (2)
89 no use of drugs or medication that could interfere with MEG/MRI signals. The
90 study complied with the Declaration of Helsinki and was approved by the local
91 Ethics Committee. All participants gave written informed consent. The details
92 regarding the MRI acquisition are described in [31]. All technical details in
93 connection with the MEG device are reported in [32]. MEG pre-processing and
94 source reconstruction were performed as in [31, 25]. Briefly, the MEG registra-
95 tion was divided into two eyes-closed segments of 3:30 min each. To identify
96 the position of the head, four anatomical points and four position coils were
97 digitized. Electrocardiogram (ECG) and electro-oculogram (EOG) signals were
98 also recorded. The MEG signals, after an anti-aliasing filter, were acquired at
99 1024 Hz, then a fourth-order Butterworth IIR band-pass filter in the 0.5-48 Hz
100 band was applied. Principal component analysis was used to remove environ-
101 mental noise measured by reference magnetometers. Supervised independent
102 component analysis was adopted to clean the data from physiological artefacts,
103 such as eye blinking (if present) and heart activity (generally one component).
104 Noisy channels were identified and removed manually by an expert rater (136
105 \pm 4 sensors were kept). After this pre-processing, 47 subjects were selected for
106 this work and all further analyses were conducted on signal amplitudes of 1 min
107 in duration source-reconstructed to 84 brain regions of interest (BROI) based
108 on the Desikan-Killiany-Tourville (DKT) anatomical parcellation atlas.

109 2.2. Avalanches detection

110 To estimate neuronal avalanches we first detected the local above-threshold
111 fluctuations. That is, the source-reconstructed time series of each brain re-

112 gion was discretized in amplitude by computing the z-score, then positive and
113 negative excursions beyond a threshold were identified. The value of the am-
114 plitude threshold was set to three standard deviations ($\pm 3\sigma$ or equivalently
115 $|z| = 3$). Then the avalanches duration was assessed by considering that a neu-
116 ronal avalanche begins when, in a sequence of contiguous time bins, at least one
117 brain region is active ($|z| > 3$) and ends when all the brain regions are inactive
118 ($|z| \leq 3$) [10, 14]. Besides, the avalanche size was defined as the total number
119 of active brain regions during a given avalanche. In this work, we analyzed
120 *neuronal avalanches*, also referred through the manuscript as *salient network*
121 *events*, without implying a connection to the brain criticality hypothesis [31].

122 *2.3. Avalanches activation and co-activation matrices*

123 For each detected avalanche, we computed the activation matrix (brain re-
124 gions \times time bins) as follows. The source-reconstructed, z-scored and time
125 binned signal were binarized, such that, at any time bin, a brain region exceed-
126 ing ± 3 was set to 1 (active), and all other regions were set to 0 (inactive, see
127 Figure 2C). For each detected avalanche, we also computed the co-activation
128 matrix (brain regions \times brain regions) by assigning 1 to all the brain regions
129 recruited in that particular avalanche. Thus, the diagonal of the co-activation
130 matrix contains 1s in all the brain regions active during a given avalanche. Be-
131 sides, summation across rows (or columns) produce, in each brain region, the
132 number of co-activated regions during a given avalanche (i.e., in terms of graph
133 theory, this is known as the degree of each brain region). The mean co-activation
134 matrix shown in the Figure 6C was computed by first averaging the co-activation
135 matrices corresponding to all the neuronal avalanches detected in each subject,
136 and then, averaging the resulting matrix across all the participants.

137 *2.4. Avalanches spatiotemporal profile*

138 To characterize avalanches spatiotemporal profile, we introduce two BROI-
139 wise metrics: The *mean avalanche duration* measuring the typical duration of
140 neuronal avalanches propagating through a brain region; and the *mean avalanche*
141 *spatial extension* measuring the typical size of avalanches propagating through
142 a brain region. Specifically, we assign to each brain region the mean avalanche
143 duration (or size) computed on all the avalanches recruiting that particular
144 region. The *mean avalanche duration* and *mean avalanche spatial extension*
145 profiles shown in the Figures 1E,G were computed by first considering all the
146 neuronal avalanches detected in each subject, and then, averaging the resulting
147 profiles across all the participants.

148 *2.5. Avalanche spectral matrix*

149 For the spectral characterization of neuronal avalanches we introduce the
150 Avalanche Spectral Matrix (ASM). To obtain the ASM we first compute the
151 whitened time-frequency representation on the whole time series of each brain
152 region (see Figure 2E). Then, the whitened time-frequency maps were selectively
153 averaged across the time points corresponding to the occurrence of the neuronal

avalanche of interest. As a result, we obtain a whitened power spectrum (see Figure 2F) associated with each brain region conforming the ASM (Brain regions \times Frequency bins) for that particular neuronal avalanche. The time-frequency maps were computed as scalograms using Morlet wavelets including spectral whitening by Z_{H0} -score normalization of each frequency bin across time samples as in [33]. The ASM can be defined at the single avalanche level (see Figure 2G), by averaging all the avalanches in each subject (data not shown) and by averaging the mean ASM of each subject across all the participants (see Figures 2H and 3A,B). To assess the statistical significance of the spectral signatures associated with the neuronal avalanches, we compute pixel-level thresholding on the mean ASM with Bonferroni correction for multiple comparisons. More specifically, we computed the mean ASM on each one of the 100 B- or C-surrogate datasets (see Section 2.9). Then these 100 surrogate mean ASMs were used to compute pixel-level thresholding on the true mean ASM using a Bonferroni-adjusted two-tailed statistical threshold = $0.05 / (\text{Brain regions} \times \text{Frequency bins})$. Note that this Bonferroni correction for multiple comparisons assuming independence between adjacent spatial/frequency bins of the mean ASM is a quite conservative test, yet, the observed spectral signature in the alpha band result evident even after this stringent thresholding process (see Figure 2H).

2.6. Avalanches waveform shape

To characterize the waveform shape of neuronal avalanches we follow a BROI-wise approach. First, in each brain region we computed the average across the 200 ms signal epochs (absolute value) centered around the start time of the avalanches of interest recruiting that particular region (see gray lines in Figures 3C,D and B.11C,D). Then, we obtained the mean avalanches waveform shape by computing the average of the resulting time series across the brain regions (see the red and blue lines in Figures 3C,D and B.11C,D).

2.7. Avalanches propagation modes

To assess the avalanches starting modes we assign to each brain region the number of avalanches igniting in that particular site (e.g., see the brain region active at $\text{Time} \approx 51.581$ sec in the activation matrix shown in Figure 2C). Similarly, for the avalanches ending modes we assign to each brain region the number of avalanches extinguishing in that particular site (e.g., see the brain region active at $\text{Time} \approx 51.597$ sec in the activation matrix shown in Figure 2C). For the avalanches maximum recruitment modes we assign to each brain region the number of avalanches involving that particular site during the avalanche maximum size (e.g., see the 4 brain regions active at $\text{Time} \approx 51.591$ sec in the activation matrix shown in Figure 2C). Last, by dividing the avalanche count obtained in each brain region by the total number of processed avalanches, we obtained the mean spatial profiles for the starting, maximum recruitment and ending avalanches modes as shown in the Figures B.8 and B.12.

195 *2.8. Clustering of avalanches*

196 Neuronal avalanches were clustered according to their spectral signature by
197 using the Louvain method for community detection based on modularity max-
198 imization [34, 35]. First, the Matrix of Paired Distance (MPD) was obtained
199 by computing the Euclidean distance between the vectorized ASMs correspond-
200 ing to the neuronal avalanches of interest taken in pairs. The resulting MPD
201 (Avalanches \times Avalanches) was normalized to be in the range [0, 1], and the
202 Adjacency Matrix (AM) was computed as $AM = 1 - MPD$. Then, the Louvain
203 algorithm was repeated 100 times on the AM for resolution parameter values
204 in the range $0.5 \leq \gamma \leq 2$ [34, 36]. Optimization of modularity quality function,
205 based on the maximization of the similarity measure (z-scored Rand index) [36],
206 was achieved for resolution parameter values within the range $0.9 \lesssim \gamma \lesssim 1.1$.
207 Finally, a consensus partition was found from the 100 partitions [37, 38, 39]. For
208 the avalanches detected in our source-reconstructed MEG dataset, the Louvain
209 algorithm consistently identified two avalanche clusters with significant differ-
210 ences in terms of mean avalanche duration, size and spectral signature in their
211 mean ASM (see Figures 3, B.10 and B.11).

212 *2.9. Surrogate datasets*

213 We generated phase-randomized A-surrogate datasets, that preserve the
214 PSD in each brain region, while disrupting the phase relationships of the spectral
215 components (both within and between brain regions). For this, in each brain
216 region we implemented a frequency domain randomization procedure, which in-
217 volves taking the Discrete Fourier Transform (DFT) of the time series, adding a
218 random phase-shift in the range $[-\pi, \pi]$ on each spectral component of the DFT
219 (preserving the odd phase symmetry associated with real signals [40]), and then
220 taking the inverse DFT to obtain the surrogate signal back in the time domain
221 [41]. The 100 phase-randomized A-surrogate datasets were obtained by apply-
222 ing this procedure 100 times on each brain region independently. In addition,
223 we also generated B-surrogate datasets that randomize the phases similarly to
224 the A-surrogate, but in this case preserving both the regional PSDs and the
225 cross-spectra. For this, we follow a similar procedure as described above with
226 the difference that the same random phase-shift was applied to all the brain re-
227 gions. This implies that the phase difference between any pair of brain regions
228 in *homologous frequency components* is preserved (i.e., preservation of cross-
229 spectra). This corresponds to preserving the Pearson's correlations between
230 brain regions (see Appendix A.1). However, the B-surrogates destroy the phase
231 relationships between *non-homologous frequency components*. Finally, we gen-
232 erated 100 C-surrogate sets of avalanches by randomizing the starting time of
233 each observed avalanche and keeping unaltered all the other properties like the
234 avalanche duration and brain regions involved in each avalanche.

235 *2.10. Spectral group delay consistency measures*

236 In Appendix A.2 we introduce the pairwise complex baseband representation
237 of band-limited signals (eqs. A.7 - A.10 and A.13 - A.16) to provide analytical

238 arguments showing that the link between local above-threshold fluctuations and
 239 oscillations can be understood in terms of the group delay consistency across
 240 the spectral components (i.e., Fourier oscillatory constituents) of the neuronal
 241 activity. The spectral group delay associated with the activity of the brain
 242 region r , is defined as the rate of change of the phase $\phi_r(\omega)$ with the frequency
 243 ω computed on the Fourier spectrum of the brain activity (i.e., the DFT):
 244 $\tau_r(\omega) = -\Delta\phi_r(\omega)/\Delta\omega(\omega)$. Where the incremental phase $\Delta\phi_r(\omega)$ is defined as
 245 the phase difference between spectral components (adjacent in frequency ω)
 246 constituting the neural activity of the brain region r . The theoretical analysis
 247 presented in Appendix A.2 suggests that the spectral group delay consistency
 248 (SGDC) is an important feature linking the oscillatory properties of a signal
 249 to the above-threshold fluctuations associated with neuronal avalanches. For
 250 an in-depth and more mathematically rigorous description of the oscillatory
 251 mechanisms eliciting above-threshold fluctuations in the brain signals and the
 252 measures quantifying the SGDC, the reader is referred to Appendix A.2 and
 253 Appendix A.3. Here, we briefly introduce the SGDC measures designed to
 254 efficiently quantify this feature in experimental data as follows,

$$SGDC(r) = \frac{1}{N} \sum_{\omega} e^{-i\Delta\phi_r(\omega)} : \Delta\omega = \text{cte. across } r \quad (1)$$

$$SGDC(\omega) = \frac{1}{N} \sum_r e^{-i\Delta\phi_r(\omega)} : \Delta\omega = \text{cte. across } \omega \quad (2)$$

255 Equations 1 and 2 define the SGDC measures as the Euler transformed incre-
 256 mental phase values $\Delta\phi_r(\omega)$ averaged across the spectral components or brain
 257 regions, respectively, with N being the number of either frequency values or
 258 brain regions as appropriate. Importantly, the $SGDC(r)$ measure (Equation
 259 1) assesses the emergence of local above-threshold fluctuations from the spec-
 260 tral components constituting the activity of the brain region r , whereas the
 261 $SGDC(\omega)$ measure (Equation 2) quantifies the synchronization of the above-
 262 threshold oscillatory bursts at the frequency ω across brain regions. We also
 263 define the pairwise spectral group delay consistency (pSGDC) to quantify the
 264 burstiness and cross-regional bursts synchronization in a single measure.

$$pSGDC(r_1, r_2) = \underbrace{\left(\frac{SGDC(r_1) + SGDC(r_2)}{2} \right)}_{\text{Mean pairwise burstiness}} \underbrace{\frac{1}{N} \sum_{\omega} e^{-i(\Delta\phi_1(\omega) - \Delta\phi_2(\omega))}}_{\text{Correlation of burstiness across } \omega} : \Delta\omega = \text{cte. across } r \quad (3)$$

265 Equation 3 shows that $pSGDC(r_1, r_2)$ is a linear measure conformed by a factor
 266 quantifying the cross-regional correlation between the group delays across the
 267 frequency values, weighted by a coefficient quantifying the burstiness of the two
 268 involved brain regions (r_1, r_2). Unless otherwise specified the SGDC and pSGDC
 269 measures were computed on the whole time series of each brain region (i.e., non-
 270 time-resolved approach). That is, we first obtain the phase values corresponding

271 to the Fourier spectral components by computing the DFT (via the Fast Fourier
272 Transform algorithm) on the whole time series of each brain region. Then,
273 SGDC and pSGDC measures were computed on the incremental phase $\Delta\phi_r(\omega)$
274 obtained as the phase difference between the Fourier spectral components taken
275 in adjacent pairs across the frequency ω . In particular, this non-time-resolved
276 approach was used to produce the results shown in the Figures 6 and B.9. On
277 the other hand, in Figure B.10 we follow a time-resolved approach. That is, the
278 $SGDC(\omega)$ array was computed in each detected avalanche by considering the
279 brain regions and time interval associated with each particular avalanche. Then,
280 the $SGDC(\omega)$ arrays were averaged selectively across the avalanches segregated
281 in the two clusters produced by the Louvain algorithm (see Section 2.8 and
282 Figure B.10).

283 3. RESULTS

284 3.1. Statistical, spatiotemporal, and spectral characterization of neuronal avalanches

285
286 We identified neuronal avalanches in our dataset and studied their characteristic
287 signatures. In particular, we introduced a comprehensive array of features
288 describing the statistical, spatiotemporal and spectral properties of neuronal
289 avalanches. Traditionally, neuronal avalanches are described in terms of the
290 distribution of their sizes and durations, which follow fat-tailed distributions
291 (Figures 1A,C). The study of these distributions is generally used to assess
292 the dynamical regime where the brain dynamics are idling (often implied to be
293 around a critical point). However, it is also informative to describe how neuronal
294 avalanches propagate through the brain regions of interest (BROI) by assessing
295 their spatial, temporal, and spectral signatures. To characterize the spatiotem-
296 poral profiles of avalanches, we introduce two BROI-wise metrics (see Methods,
297 Section 2.4): The *mean avalanche duration* measures the typical duration of
298 neuronal avalanches propagating through a brain region (Figures 1E,F); and
299 the *mean avalanche spatial extension* measures the typical size of avalanches
300 propagating through a brain region (Figures 1G,H). The brain plots in Figures
301 1F,H reveal a characteristic topography, demonstrating the heterogeneous role
302 that each brain region plays in the propagation of neuronal avalanches. Next, we
303 introduce a tool to characterize the spectral signature of neuronal avalanches,
304 by first transforming the regional signals into a time-frequency representation
305 and then averaging the time-frequency content selectively across the time points
306 corresponding to the occurrence of each neuronal avalanche (Figures 2E,F). This
307 way, we defined the spectral fingerprint of each neuronal avalanche, which we
308 named Avalanche Spectral Matrix (ASM, see Methods). Figure 2 displays the
309 ASM for a single avalanche (panel G) and averaged across all subjects (panel
310 H). Figure 2H shows that the frequency content of most brain regions peaks in
311 the alpha band (8-13 Hz) during neuronal avalanches. In other words, during
312 salient network events, brain regions fluctuate predominantly in alpha. This is
313 also observed away from the occipital regions, suggesting that synchronization

in the alpha band might spread on a large-scale during neuronal avalanches (see in Section 3.6 the discussion of the results shown in Figure B.10). Note that this result provides a relevant insight regarding the connection between salient network events and narrowband oscillations and, it is non-trivial since neuronal avalanches are rare phenomena, occupying only a small fraction of the total recording (in space and time), generally around 1% of time points. The ASM can be defined at the single avalanche level (Figure 2G). Thus, we asked if avalanches with different spectral signatures propagate differently. In particular, we hypothesized a relationship between the avalanche spectral signature (ASMs) and the avalanche duration and extension, as defined above. To test this relationship, we clustered neuronal avalanches according to their ASM using the Louvain algorithm (see Methods). We found that avalanches cluster into two main groups based on their frequency content (Figures 3A,B). Importantly, we found a statistically significant difference of the mean avalanches duration and size between cluster 1 and cluster 2 (see Figures 3E,H). For this, in each brain region we computed a non-parametric permutation test (random sampling without replacement, 1×10^4 permutations). All the brain regions disclosed a statistically significant difference of the mean avalanches duration and size between cluster 1 and 2 (the Bonferroni-adjusted two-tailed P values result $P < 0.001$ in all the brain regions). The avalanches belonging to cluster 1 (Figure 3A) display a less marked and less widespread alpha peak in the ASM as compared to cluster 2 (Figure 3B). Consistently, the two clusters are also well distinguished by their different waveform shapes, with group 1 showing shorter temporal profiles of above-threshold fluctuations. Figures 3C,D show the average waveform shapes of avalanches, obtained by averaging in each brain region (BR) the absolute value of the time series associated with each neuronal avalanche (see Methods). These results suggest that cluster 2 avalanches is specifically related to the long-range spread of narrowband alpha bursts across the brain network, whereas cluster 1 avalanches correspond to more spatially localized fluctuations mainly promoted by the broadband $1/f$ activity (see Figures 3E-J). The two identified clusters are also characterized by different avalanche duration and size, which confirms our hypothesis. In particular, cluster 1 avalanches are generally small and short-lived when compared to cluster 2 avalanches (see Figures 3E,H,G,J), although both clusters display avalanche size and duration distributions spanning across a few orders of magnitude (see Figures 3G,J). Interestingly, the slope of the fat-tailed distributions is different in the two clusters, which could have implications for the study of power-law statistics related to the criticality hypothesis. We also found that avalanches propagate in a cluster-specific manner (see Figure B.8 in Appendix B.2) That is, the spatial profiles associated with the start and end of each avalanche cluster disclose a high correlation between the two clusters (see Figures B.8A-C and Figures B.8G-I), whereas a different scenario is observed in terms of how the brain regions are recruited by the two avalanche clusters. Specifically, brain regions that are recruited by the longer avalanches of cluster 1, will be recruited by the shorter avalanches of cluster 2, and vice versa (see Figure B.8D). Within cluster 1, the longest avalanches occupy the frontal and

360 occipital regions (see Figure B.8E), whereas in cluster 2, associated with the
361 spectral signature in the alpha band, the longest avalanches are in the parietal and temporal regions (see Figure B.8F). The opposite trend is observed
362 for the shortest avalanches. In fact, performing Pearson's correlations between
363 the spatial profiles of cluster 1 and cluster 2 corresponding to the maximal
364 size of recruitment across brain regions, we obtain a strong negative correlation
365 ($r = -0.841$, $P < 0.001$ two-tailed Student's t-test, see Figure B.8D). Note that
366 the specificity of cluster 2 avalanches, associated with transient above-threshold
367 alpha bursts, in recruiting parietal and temporal brain regions can not be trivially
368 explained by the presence of elevated (steady) alpha oscillatory power,
369 which is commonly observed in occipital brain regions during the eyes-closed
370 resting state (see Figure 2B). In summary, in this section we have introduced a
371 comprehensive array of avalanche features, showing that rare, short-lived salient
372 network events propagating across the brain during spontaneous resting state
373 activity are highly structured in terms of their spatial, temporal, and spectral
374 properties. In particular, the spectral characterization using the ASM provided
375 relevant insights regarding the connection between the observed salient network
376 events and narrowband oscillations in the alpha band.
377

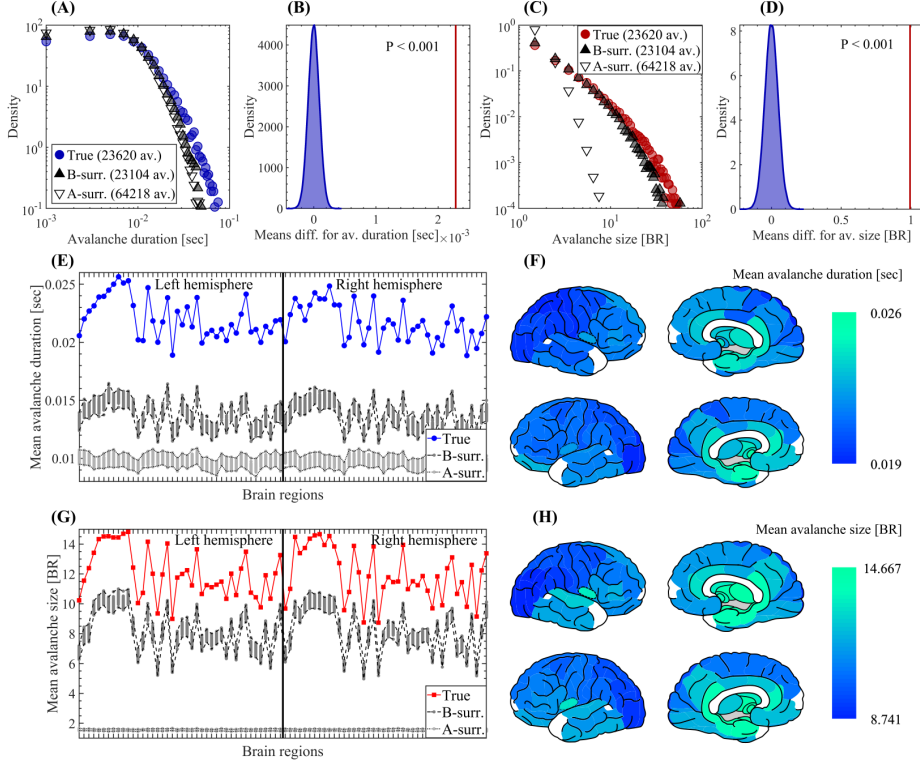


Figure 1: Statistical and spatiotemporal characterization of neuronal avalanches. (A) Distribution of the duration of neuronal avalanches observed in the true source-reconstructed MEG data (filled blue circles), the A-surrogate (empty down-pointing triangles) and the B-surrogate (filled up-pointing triangles). In the three cases the avalanches were computed on the 47 participants. The distributions of avalanches duration for the true MEG data and the B-surrogate disclose a statistically significant difference ($P < 0.001$, two-sample Kolmogorov-Smirnov test). (B) Results of the non-parametric permutation test. Histogram corresponding to the sampling distribution of the difference between the means of the true and B-surrogate distributions of avalanches duration. The histogram was computed via random sampling without replacement (1×10^5 permutations). The red vertical line in the histogram indicates the actual mean difference between the true and B-surrogate distributions of avalanches duration. The two-tailed P value is reported. (C) Same as in A for the size of neuronal avalanches. The distributions of avalanches size for the true MEG data and the B-surrogate disclose a statistically significant difference ($P < 0.001$, two-sample Kolmogorov-Smirnov test). (D) Same as in B for the size of neuronal avalanches. (E) Spatial profile showing the mean duration of neuronal avalanches propagating through each brain region (mean value across the 47 participants, see Methods). (F) Brain topographies for the mean duration of neuronal avalanches as shown in panel E. (G) Same as in E for the size of neuronal avalanches. (H) Same as in F for the size of neuronal avalanches. Symbols and abbreviations: BR, Brain Regions.

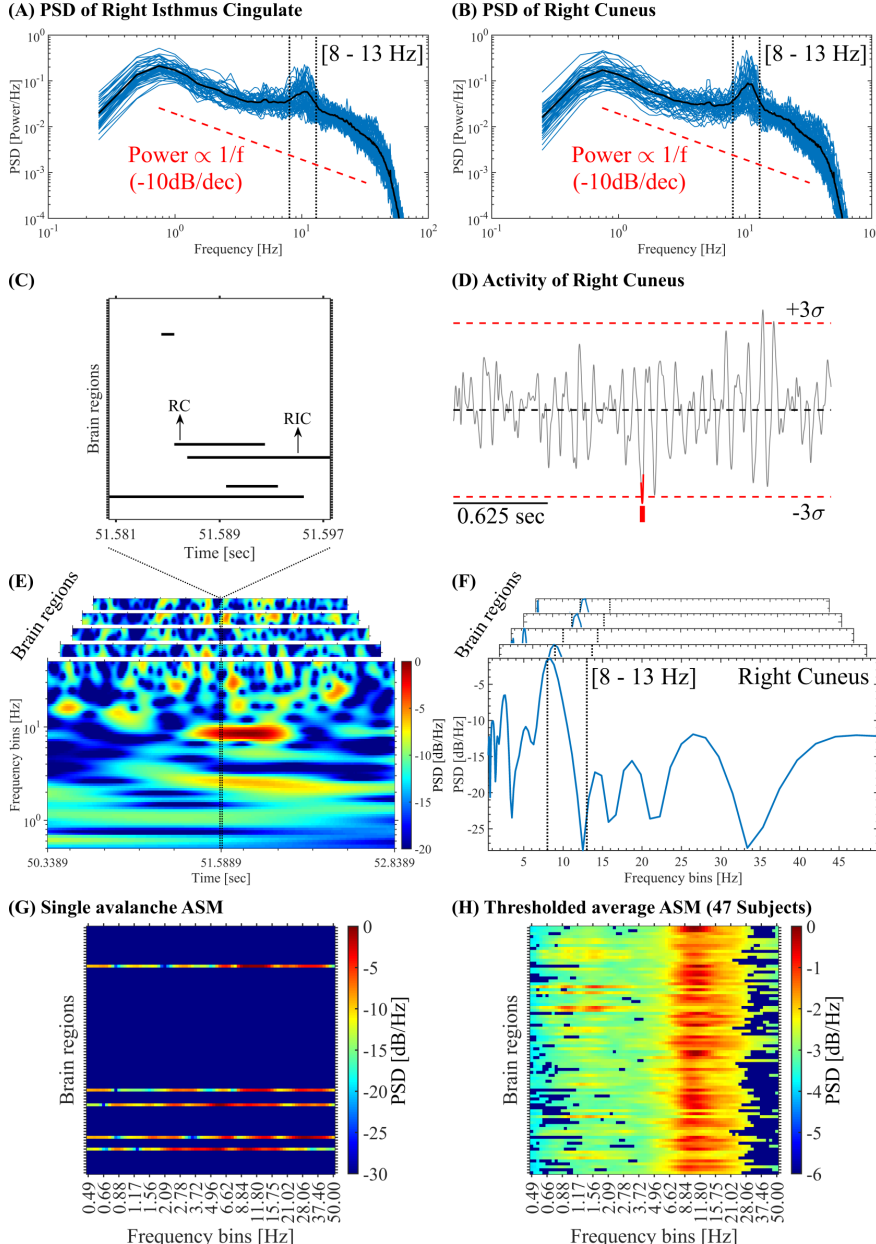


Figure 2: Avalanche Spectral Matrix. (A, B) Power spectra computed on the Right Isthmus Cingulate (RIC, panel A) and the Right Cuneus (RC, panel B) activities (1 min length) of each patient (blue lines) and the resulting average (black line). Note that the PSDs of the RC (panel B) disclose a prominent bump in the alpha band (8-13 Hz) characteristic of the occipital brain regions, however, a less prominent bump in the alpha band is also observed in regions away from the occipital cortex (see the PSDs of RIC shown in panel A). (C) Activation matrix of a single avalanche showing the time intervals in which each brain region was active (i.e., absolute amplitude $> 3\sigma$). (D) Activity of the RC disclosing the above-threshold fluctuation (highlighted in red) associated with the brain avalanche shown in panel C. (E) Whitened time-frequency maps (see Methods) of each brain region involved in the avalanche shown in panel C. (F) Whitened power spectra associated with each brain region involved in the avalanche shown in panel C. The vertical dotted lines indicate the alpha band. To build the ASM, we average the whitened time-frequency content selectively across the time samples corresponding to the occurrence of each neuronal avalanche. As a result, we obtain a whitened power spectrum for each brain region. (G) ASM corresponding to the neuronal avalanche shown in panel C. (H) Mean ASM resulting from the average across all the avalanches detected in the 47 subjects, and then, Bonferroni-thresholded using the B-surrogate (see Methods). Symbols and abbreviations: ASM, Avalanche Spectral Matrix; PSD, Power Spectral Density; RC, Right Cuneus; RIC, Right Isthmus Cingulate.

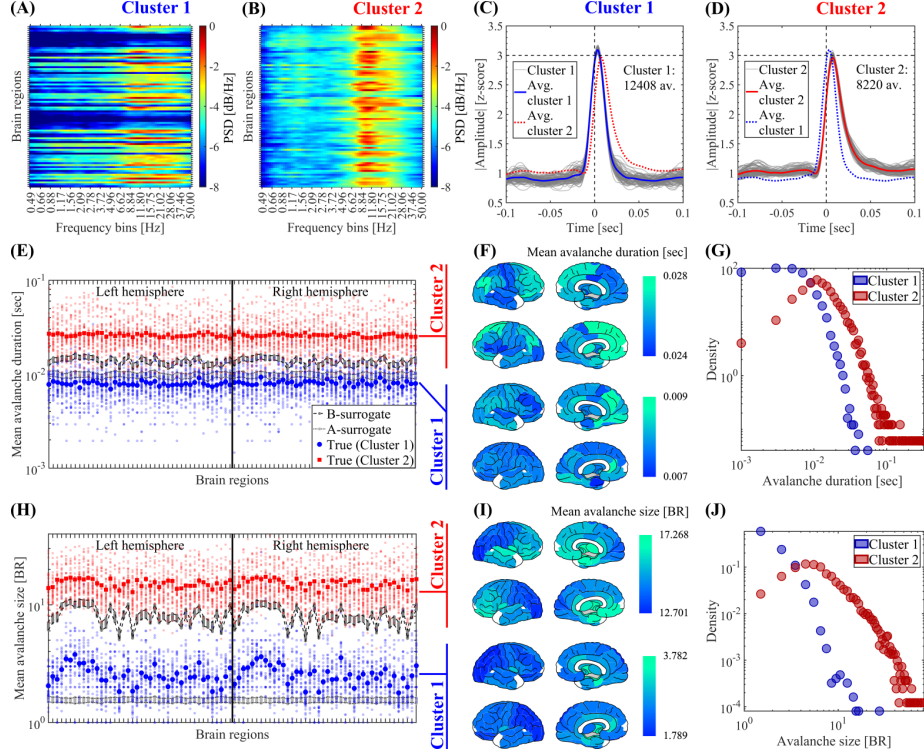


Figure 3: Clustering of avalanches according to spectral signature. The avalanches obtained from 41 subjects were clustered using the Louvain algorithm (resolution parameter $\gamma = 1$, see Methods). (A, B) Mean ASM of the two avalanches clusters identified by the Louvain algorithm computed on the avalanches detected in the 41 participants. (C, D) Waveform shapes of the avalanches pertaining to the two avalanches clusters identified by the Louvain algorithm. Thin gray lines correspond to the average waveform shape in each brain region. Thick blue and red lines correspond to the resulting waveform shape averaged across the brain regions for avalanche cluster 1 and 2, respectively. (E) Spatial profile showing the mean duration of avalanches pertaining to cluster 1 (in blue) and cluster 2 (in red). For the true data, the small and big markers correspond to the mean spatial profile in each patient and the average across the 41 participants, respectively (see Methods). To test the significance of the difference of the mean avalanches duration between cluster 1 and cluster 2, in each brain region we computed a non-parametric permutation test (random sampling without replacement, 1×10^4 permutations). All the brain regions disclosed a statistically significant difference of the mean avalanches duration between cluster 1 and 2 (the Bonferroni-adjusted two-tailed P values result $P < 0.001$ in all the brain regions). (F) Brain topographies for the mean duration of neuronal avalanches averaged across the 41 participants as shown in panel E. (G) Distribution of the duration of avalanches pertaining to the cluster 1 and cluster 2 observed in the 41 participants. (H) Same as in E for the size of neuronal avalanches. To test the significance of the difference of the mean avalanches size between cluster 1 and cluster 2, in each brain region we computed a non-parametric permutation test (random sampling without replacement, 1×10^4 permutations). All the brain regions disclosed a statistically significant difference of the mean avalanches size between cluster 1 and 2 (the Bonferroni-adjusted two-tailed P values result $P < 0.001$ in all the brain regions). (I) Same as in F for the size of neuronal avalanches. (J) Same as in G for the size of neuronal avalanches. Symbols and abbreviations: BR, Brain Regions.

378 3.2. *Neuronal avalanches and phase coherence: surrogate data analysis*

379 During neuronal avalanches, the signals display large deviations from the
380 baseline, which are coordinated across regions, giving rise to complex activation
381 patterns with well-defined statistical, spatiotemporal, and spectral features.
382 In this work, we hypothesize that the presence of narrowband oscillations,
383 broadband $1/f$ activity, and transient synchronization across the spectral
384 components of brain signals, both locally in a region and globally across
385 brain regions, are necessary conditions for the emergence of realistic neuronal
386 avalanches. A common way to test the necessary and/or sufficient conditions
387 underlying a phenomenon (here, neuronal avalanches) is the use of surrogate
388 data analysis. This approach involves creating surrogate datasets that remove
389 or alter a specific property (e.g., phase relationships) while preserving other
390 statistical characteristics, allowing one to determine if the absence or modifi-
391 cation of the property affects the observed feature of interest. Following this
392 line of reasoning, we generated 100 phase-randomized "A-surrogate" datasets
393 (see Methods), that preserve the PSD in each brain region, while disrupting
394 the phase relationships of the spectral components (both within and between
395 brain regions). Despite the A-surrogates having the same spectral content as
396 the original data, they do not disclose fat-tailed distributions of avalanche size
397 and duration (see A-surrogates in Figures 1A,C), nor realistic spatiotemporal
398 patterns of propagation (see A-surrogates in Figures 1E,G) and ASMs (data not
399 shown). Another hypothesis to rule out is that the avalanche properties shown
400 in Figure 1 could be ascribed to the static correlations between signals (which
401 are not preserved by the A-surrogates). To test this hypothesis, we generated
402 100 phase-randomized B-surrogate datasets (see Methods) that randomize the
403 phases similarly to the A-surrogate, but in this case preserving both the re-
404 gional PSDs and the cross-spectra. The preservation of cross-spectra implies
405 that the phase difference between any pair of brain regions in *homologous fre-*
406 *quency components* is preserved. This corresponds to preserving Pearson's cor-
407 relations between brain regions (see Appendix A.1). However, the B-surrogates
408 destroy the phase relationships between *non-homologous frequency components*.
409 As shown in Figure 1, the observed distributions of avalanches duration and
410 size (Two-sample Kolmogorov-Smirnov test: $P < 0.001$ for panels A and C),
411 mean spatiotemporal properties (see B-surrogates in panels E, G and the results
412 of permutation test shown in panels B and D), and ASMs (see Figure 2H) are
413 not explained by the B-surrogates. Notice that these results are non-trivial,
414 since in both the original and the B-surrogate datasets the number of neuronal
415 avalanches is almost identical, and large events are also observed in the surro-
416 gate data (see B-surrogates in Figures 1A,C). To summarize, despite retaining
417 the same power spectra and cross-spectra, the loss of synchronization across
418 spectral components (given by the phase randomization), impairs large-scale
419 coordinated salient network events, significantly disrupting the statistics and
420 features of neuronal avalanches.

421 3.3. *Neuronal avalanches, narrowband oscillations and broadband 1/f activity:*
422 *modeling insights*

423 We built a signal model to elucidate the relation between neuronal avalanches,
424 narrowband oscillations, and broadband 1/f activity. We model the activity of
425 single brain regions as the linear superposition of Fourier components oscillating
426 in a narrow frequency band. As a result, the corresponding spectral representa-
427 tion discloses a "bump" of (null-to-null) bandwidth in the alpha band (8-13 Hz,
428 Figures 4A,D,G). The broadband arrhythmic activity was modeled by imposing
429 a 1/f trend in the PSD of each signal (Figure 4G). This 1/f spectral background
430 was chosen to mimic the $-10dB/dec$ log-log decay rate observed in the PSDs as-
431 sociated with true data (see Figures 2A,B). To model different degrees of phase
432 coherence, we assign random phase values to the spectral components within a
433 range $[-\epsilon\pi, \epsilon\pi]$ with $\epsilon \in [0, 1]$ (see right panels in Figures 4A,D,G). On the one
434 hand, for $\epsilon \simeq 1$, the spectral components of the signal were desynchronized (i.e.,
435 independent oscillatory components, Figure 4A). On the other hand, for $\epsilon \simeq 0$
436 the spectral components were highly synchronized (i.e., high cross-frequency
437 coherence). We first focused on a *single brain signal* and measured the num-
438 ber of salient events (i.e., transient excursions of the amplitude above a fixed
439 threshold of 3 standard deviations: $\pm 3\sigma$) depending on the presence or absence
440 of coherent oscillations and 1/f activity (see Figures 4C,F,I). In the absence of
441 1/f activity and for uniformly distributed random phases assigned to the spec-
442 tral components in the alpha band ($\epsilon = 1$, Figures 4A), the model displays very
443 few above-threshold fluctuations across trials (Figures 4B,C). Increasing the co-
444 herence of the spectral components in the alpha band ($\epsilon = 0.75$, Figures 4D),
445 despite the absence of 1/f activity, the number of above-threshold fluctuations
446 increased, producing a salient burst in most of the trials (Figures 4E,F). Finally,
447 the presence of the broadband 1/f activity with $\epsilon = 1$ and coherent spectral
448 components in the alpha band with $\epsilon = 0.75$ (Figure 4G) further increased the
449 number of salient events in a single brain signal (Figures 4H,I). Importantly,
450 the 1/f activity also influences the rhythmicity of above-threshold fluctuations,
451 which occur aperiodically. More specifically, if we synthesize a long time series
452 by concatenating trials constructed without the 1/f activity (as in Figures 4E),
453 the concatenated time series will disclose a periodic series of above-threshold
454 alpha bursts (i.e., one salient alpha burst per trial). Instead, in the presence
455 of 1/f activity we obtain above-threshold fluctuations occurring at random in
456 each trial besides the salient alpha burst, hence, the time series resulting from
457 concatenating trials (as in Figure 4H) will disclose an aperiodic series of above-
458 threshold fluctuations. In summary, these results suggest that the mere presence
459 of oscillations associated with an increase of power around a narrow frequency
460 band does not guarantee the stable occurrence of above-threshold fluctuations
461 (Figures 4A-C). However, if the phases of the spectral components are coher-
462 ent, then high-amplitude fluctuations are consistently observed in the signal
463 (Figures 4D-F). Furthermore, a specific relationship between the amplitudes of
464 the narrowband oscillations and the broadband arrhythmic component is nec-
465 essary for the resulting local activity to exhibit realistic aperiodically occurring
466 above-threshold fluctuations (see regime R2 in Figure 4I).

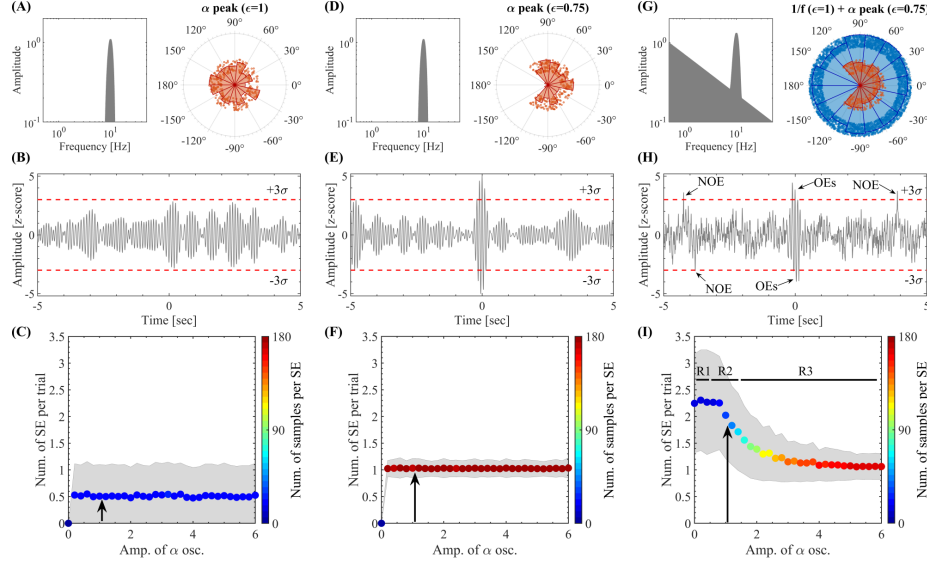


Figure 4: Model for local above-threshold fluctuations. (A) Amplitude spectrum (left) and distribution of the phase values assigned to the spectral components (right) for the oscillatory activity in the alpha band (Hann window with null-to-null bandwidth = 8-13 Hz, frequency resolution $df = 1/60\text{sec} \approx 0.017\text{ Hz}$). Random phases were assigned to all the spectral components within the range $[-\epsilon\pi, \epsilon\pi]$ with a phase factor $\epsilon = 1$. (B) 10 sec epoch extracted from the synthetic time series produced by the amplitude spectrum and phase distribution shown in panel A (sampling rate of $f_s = 1024\text{ Hz}$). The horizontal dashed lines in red indicate the 3 standard deviations ($\pm 3\sigma$) thresholds used to compute the salient events as above-threshold amplitude fluctuations. (C) Number of salient events (SE) per trial as a function of the maximum amplitude value of the oscillatory activity in the alpha band. For each maximum amplitude value, we counted the number of SE across 1000 trials of 10 sec in length (trials) synthesized as the one shown in panel C. In each trial, we recomputed the random phases of the spectral components within the range $[-\epsilon\pi, \epsilon\pi]$ with $\epsilon = 1$. The colored markers indicate the mean number of SE per trial across the 1000 trials. The shaded error bars in gray correspond to the standard deviation around the mean value. The pseudocolor scale represents the mean value for the number of above-threshold samples per salient event. The black arrow indicates the maximum amplitude of the alpha oscillations used in panels A and B. (D-F) Same as in A-C for spectral components with random phases constrained within the range $[-\epsilon\pi, \epsilon\pi]$ with $\epsilon = 0.75$ (see the distribution of the phase values in panel D). (G) Amplitude spectral profile (left) resulting from the linear superposition of 1) a narrowband amplitude spectrum around the alpha band (Hann window with null-to-null bandwidth = 8-13 Hz), and 2) a set of spectral components with power $A^2(f) \propto 1/f$ (frequency resolution $df = 1/60\text{sec} \approx 0.017\text{ Hz}$). The right side of panel G shows the distribution of phase values assigned to the spectral components. Random phases within the range $[-\epsilon\pi, \epsilon\pi]$ with $\epsilon = 1$ where assigned to the spectral components constituting the $1/f$ background (blue circles) and $\epsilon = 0.75$ where assigned to the spectral components associated with the alpha bump (red circles). (H) Same as in B and E for the spectrum shown in panel G. In this case, it is possible to distinguish oscillatory (OEs) and non-oscillatory (NOEs) salient events. R1, R2 and R3 indicate regions characterized by *Amp. of alpha oscillations* less than, approx. equal to and greater than the *Amp. 1/f activity*, respectively. Symbols and abbreviations: SE, Salient Events.

467 Next, we extended the above setup to model *whole-brain activity* and neuronal
 468 avalanches. For each simulated brain signal, we set the amplitude of the

alpha peak proportionally to that observed in empirical MEG recordings (with alpha amplitude $\in [0, 1]$), thus modeling the non-homogeneous presence of alpha activity across brain regions. In addition, in each region, we bounded the random phases assigned to the spectral components in the alpha band within a range $[-\epsilon\pi, \epsilon\pi]$, whose width $\epsilon \in [0.75, 1]$ was inversely proportional to the empirical alpha power (i.e., the higher the alpha peak, the higher the phase coherence among the spectral components). This choice was motivated by the fact that high PSD bumps are generally interpreted as stronger narrowband synchronization within local neuronal populations [42] (see Discussion). Using this setup, we measured synthetic neuronal avalanches and tested their dependence on the $1/f$ activity. When only alpha oscillations were present, and no broadband $1/f$ activity (Figure 5A), the ASM was not realistic compared to the empiric one (Figure 5B), and the distribution of avalanche durations and sizes was not following a linear trend in log-log plots (Figures 5C,D). Instead, when only broadband $1/f$ activity was present, and no oscillatory activity in the alpha band nor coherent phase values were used (i.e., $\epsilon = 1$; Figure 5E), the ASM did not show the spectral signature associated with the alpha component (Figure 5F). Also, the distribution of avalanche durations was similar to the empirical data, while the distribution of avalanche sizes was shrunk, as the model did not display events involving large populations (Figures 5G,H). Finally, when both broadband $1/f$ activity and alpha oscillations were simultaneously present (Figure 5I), the emerging neuronal avalanches displayed a realistic ASM (compare Figure 5J with Figures 2H) as well as fat-tailed distributions of durations and sizes (Figures 5K,L); although the sizes decayed in a markedly more rapid fashion than in the empirical data (compare Figures 5K,L with Figures 1A,C). These results suggest that both narrowband oscillations and broadband $1/f$ spectral background contribute to the signal deviations from baseline activity and realistic neuronal avalanches, provided that the narrowband spectral components display appropriate levels of phase coherence.

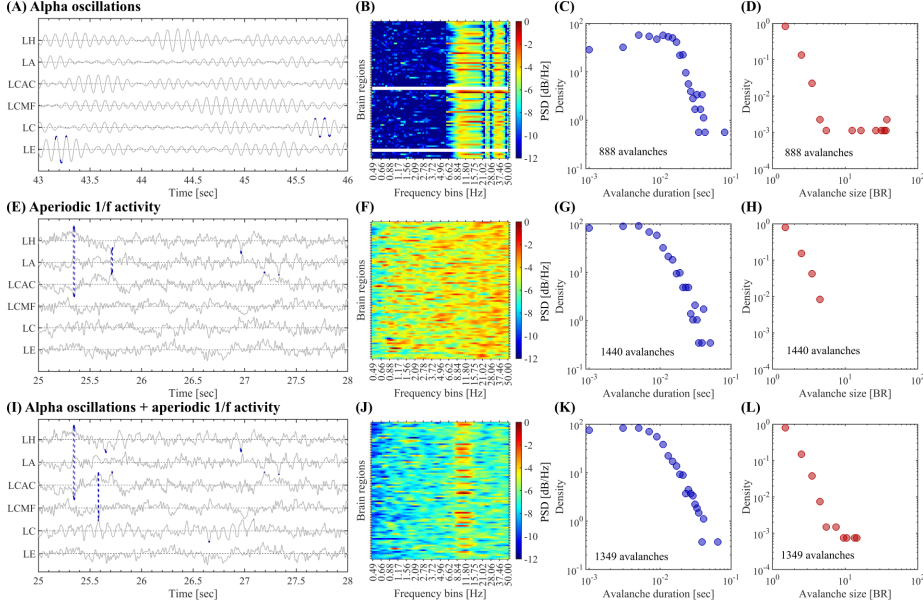


Figure 5: Large-scale model for neuronal avalanches. (A-D) Large-scale model for neuronal avalanches including only alpha oscillations (random phase values in the alpha band constrained to the range $[-\epsilon\pi, \epsilon\pi]$ with $\epsilon \in [0.75, 1]$). Panel A shows a subset of synthetic activities. In each time series, the above-threshold fluctuations ($\pm 3\sigma$) are highlighted in dark blue. Vertical dashed lines connect the activations constituting avalanches completely contained in the subset of signals shown. Panel B shows the resulting ASM averaged across the avalanches. Panels C and D show the distribution of avalanche duration and size, respectively. Panels A-C were computed on all the avalanches detected in a simulated time series of 1 min in length. (E-H) Same as in A-D for the large-scale model including only broadband 1/f activity, and no oscillatory activity in the alpha band nor phase consistency values were present ($\epsilon = 1$). (I-L) Same as in A-D for the large-scale model including both broadband 1/f activity with non-constrained random phases ($\epsilon = 1$) and alpha oscillations with random phases constrained proportionally to the observed alpha power in the range ($\epsilon \in [0.75, 1]$). Symbols and abbreviations: LH, Left Hippocampus; LA, Left Amygdala; LCAC, Left Caudal Anterior Cingulate; LCMF, Left Caudal Middle Frontal; LC, Left Cuneus; LE, Left Entorhinal.

498 3.4. Spectral group delay consistency underlies local above-threshold fluctuations

499

500 In the present and the next sections, we provide a unifying rationale for the
 501 mechanisms underlying the empiric and model evidence presented in Sections
 502 3.1, 3.2 and 3.3. Here, we present the analytical arguments showing that the link
 503 between local above-threshold fluctuations and oscillations can be understood in
 504 terms of the group delay consistency across the spectral components constitut-
 505 ing the brain activity. In particular, we found that the magnitude of the phase
 506 factor ϵ , associated with the results shown in Figure 4, creates above-threshold
 507 fluctuations by affecting the spectral group delay $\tau(\omega) \approx -\Delta\phi(\omega)/\Delta\omega$, defined
 508 as the rate of change of the phase $\phi(\omega)$ with the frequency ω computed on the
 509 Fourier spectrum of the brain activity (i.e., the DFT). We studied this phe-
 510 nomena using both numerical (Figures B.6 and B.7) and analytically tractable

(Figures A.1 and A.2) modeling examples. For the analytical approach, we used the complex baseband representation of signals based on grouping the Fourier spectral components in (non-overlapping) pairs adjacent in frequency. In this representation, the time series of interest is decomposed as a linear superposition of amplitude modulated components (see Figures A.1E,J and A.2E,J and the synthesis equations A.7 - A.10 and A.13 - A.16). Essentially, when all the Fourier spectral components are added together to synthesize the signal in the time domain (i.e., the inverse DFT), the spectral group delay determines the time alignment of the amplitude envelope associated with each pair of adjacent spectral components (see the amplitude modulated components in Figures A.1E,J and A.2E,J). Such time alignment promotes transient large-amplitude excursions of the signal (i.e., above-threshold fluctuations). Specifically, for adjacent spectral components having highly dissimilar phase values disclosing a nonlinear dependence with the frequency ω (e.g., random phase values with $\epsilon \simeq 1$ as shown in the right panel of Figure 4A), the resulting spectral group delay depends on ω (see Figures A.1H and A.2H). In this case, we say that the signal has low spectral group delay consistency (SGDC) which reduces the occurrence of above-threshold fluctuations (see Figures A.1J and A.2J). Instead, in the case of adjacent frequency bands with phase values depending linearly with ω or having phase values disclosing a nonlinear dependence with ω but constrained within a small phase range (e.g., random phase values with $\epsilon \simeq 0.75$ as shown in the right panel of Figure 4D), we obtain approximately constant group delay values for all the pairs of adjacent spectral components (see Figures A.1C and A.2C). In such a case, the signal has a high SGDC which promotes the occurrence of above-threshold fluctuations (see Figures A.1E and A.2E). The numerical results shown in the Figure B.6 confirm these findings in the case of the signal model for local above-threshold fluctuations. Specifically, Figure B.6 shows that the increase of the signal burstiness, as quantified by the kurtosis, associated with more constrained random phase values (i.e., low phase factor ϵ values) is explained by the increase in the SGDC as quantified by the $SGDC(r)$ measure. Importantly, we re-compute the signal model for the same set of phase factor values used in Figure B.6, this time using spectral phase values disclosing not a random but a linear dependence with the frequency (i.e. a time-shift). The results obtained with this configuration are shown in Figure B.7. As predicted by the spectral group delay mechanism (see Figures A.1A-E), we obtained $|SGDC(r)| \approx 1$ independently of the phase factor value ($\epsilon \in [0, 1]$), and the time series produced by the signal model disclosed (time-shifted) above-threshold fluctuations in all the cases (see Figure B.7). These numerical results constitute further evidence showing that the SGDC effectively underlies the emergence of local above-threshold fluctuations from narrowband oscillations. For an in-depth and more mathematically rigorous description of this mechanism, the reader is referred to Appendix A.2. To quantitatively study the effects of SGDC on our data we introduce specialized measures (see Methods and Appendix A.3). The $SGDC(r)$ is bounded in the range $[0, 1]$ and quantifies how much the group delay varies across the spectral components associated with the signal of interest (see Equation 1). In Appendix A.3 we show the performance of

557 the $SGDC(r)$ measure in assessing the emergence of local above-threshold fluc-
558 tuations from the Fourier oscillatory components of synthetic signals (see Figure
559 A.3). Importantly, we found that the $SGDC(r)$ measure discloses a significant
560 positive correlation with the number of observed above-threshold fluctuations
561 ($r = 0.184$, $P < 0.001$ two-tailed Student's t-test, see Figure B.9G), implying
562 that in our MEG dataset a significant fraction of the local salient events are
563 above-threshold oscillatory bursts associated with high SGDC (mainly in the
564 alpha band). Taken together, these results suggest that the emergence of lo-
565 cal above-threshold fluctuations from the Fourier oscillatory constituents of the
566 brain activity can be understood in terms of the SGDC as quantified by the
567 $SGDC(r)$ measure.

568 3.5. *Spectral group delay consistency, transient cross-regional coherent oscilla-*
569 *tions and broadband 1/f activity underlie neuronal avalanches*

570 In Sections 3.3 and 3.4, we have shown that the concurrent presence of broad-
571 band 1/f activity and narrowband oscillations disclosing appropriate levels of
572 SGDC, are two key ingredients sufficient to generate realistic above-threshold
573 fluctuations in a single brain signal. In this section, we present the rationale and
574 results pointing out that SGDC is a key conceptualization also in connection
575 with the emergence of realistic neuronal avalanches as a collective phenomena
576 involving multiple brain regions. Firstly, in Appendix A.4 we provide a theo-
577 retical approach showing that the data-driven results presented in Section 3.2
578 associated with the A- and B-surrogates can be understood in terms of SGDC
579 properties. We analytically found that, despite of preserving the power spec-
580 trum (which includes alpha oscillations and broadband 1/f activity), the phase
581 randomization associated with both A- and B-surrogates significantly reduces
582 the burstiness of each brain region (i.e., occurrence of above-threshold fluctua-
583 tions) as assessed by the $SGDC(r)$ measure (see Appendix A.4). This reduction
584 in the $SGDC(r)$ magnitude provides a theoretical argument underpinning the
585 evidence showing that A- and B-surrogates failed to reproduce realistic neu-
586 ronal avalanches (see Section 3.2). Moreover, our empirical results show that
587 A-surrogates perform worst than B-surrogates in reproducing realistic neuronal
588 avalanches (see Figure 1). This evidence is consistent with the analytical deriva-
589 tions presented in Appendix A.4 showing that B-surrogates preserve the original
590 magnitude of the $SGDC(\omega)$ measure, and only A-surrogates destroy both the
591 burstiness of each brain region (as assessed by the $SGDC(r)$ measure) and the
592 synchronization of above-threshold fluctuations across brain regions (as assessed
593 by the $SGDC(\omega)$ measure). Secondly, the spectral signature in the alpha band
594 disclosed by the averaged ASMs associated with the neuronal avalanches ob-
595 served in our MEG data (see Figure 2H), suggests that coherence in the alpha
596 band occurring in a transient manner across brain regions is also an essential
597 feature of the realistic avalanches. To test this, we generated 100 C-surrogate
598 sets of avalanches (see Methods) that randomize the starting time of each ob-
599 served avalanche and keep unaltered all the other properties like the time width
600 and brain regions involved in each avalanche. Figures B.10A and B.10B show

the average ASMs corresponding to the true and C-surrogate avalanches computed on 10 subjects, respectively. In particular, Figure B.10B shows that the alpha signature is barely distinguishable in the average ASM corresponding to the C-surrogate avalanches. Importantly, as shown in the Figure B.10C, the average ASM of the true avalanches thresholded with the average ASM of the C-surrogate avalanches (see Methods) discloses a prominent spectral signature in the alpha band. As a conclusion, these results suggest that the large-scale spreading of alpha bursts occurs mainly via brain avalanches. Although the $SGDC(r)$ measure assesses the emergence of above-threshold fluctuations from the Fourier oscillatory constituents of the activity associated with a single brain region, it does not account for cross-regional effects associated with neuronal avalanches. To quantitatively study the cross-regional effects of SGDC on our data we introduce the $SGDC(\omega)$ measure. The $SGDC(\omega)$ is bounded in the range $[0, 1]$ and quantifies how much the group delay at a given frequency ω varies across brain regions (see Equation 2). In Appendix A.3 we show the performance of the $SGDC(\omega)$ measure in assessing the emergence of above-threshold fluctuations synchronized across brain regions (see Figures A.4 and A.5). Figures B.10D and B.10E show the average ASMs of the two avalanche clusters identified by the Louvain algorithm (see Methods) computed on 10 subjects. Importantly, the Figure B.10F shows the increase of transient cross-regional coherence around the alpha band, as quantified by the $SGDC(\omega)$ measure, associated with the avalanches disclosing the alpha spectral signature in the average ASM (i.e., avalanche cluster 2). Notably, Figure B.10G shows that the transient cross-regional coherence around the alpha band associated with the cluster 2 avalanches is also captured by the large-scale model presented in Section 3.5. In summary, these results suggest that a) spectral group delay consistency in specific narrow frequency bands (as assessed by the $SGDC(r)$ measure), b) transient cross-regional coherent oscillations (intra-frequency coherence across brain regions assessed by the $SGDC(\omega)$ measure) and c) broadband $1/f$ activity, are all key ingredients for the emergence of realistic avalanches.

3.6. Mechanisms of long-range interactions

Synchrony is thought to play a role in coordinating information processing across different brain regions. However, correlation structures such as hemodynamic functional connectivity are better explained in terms of power amplitude correlations of electrophysiological signals (e.g., MEG), rather than phase-synchrony. In a recent work, it was demonstrated that power correlation between two signals can be analytically decomposed into signal coherence (a measure of phase synchronization), cokurtosis (a measure of the probability of simultaneous large fluctuations), and conjugate-coherence [43]. In particular, it was proposed that the cokurtosis between two signals provides a measure of co-bursting that offers a robust neurophysiological correlate for hemodynamic resting-state networks [43]. Here we show that the SGDC conceptualization can be used to explain both the co-burstiness and the cokurtosis in terms of the coherence of the signals' spectral content, therefore, advancing our understanding of the mechanisms of long-range communication. For this, we counted

the co-participation of pairs of brain regions across avalanches (see Methods, Section 2.3). Figure 6C shows the number of co-activations between each pair of brain regions. Figure 6B shows the number of relative co-activations, i.e., the accumulated number of activations in each row of the co-activation matrix relative to the total number of activations in each brain region (diagonal of the co-activation matrix). Figure 6A displays the brain plots corresponding to the number of relative co-activations shown in Figure 6B. It is essential to note that the topography of co-activations shown in the Figures 6A-C can not be trivially explained by the chance co-occurrence of rare above-threshold fluctuations in the brain activity. In fact, Figure B.9 shows that even though the kurtosis (Equation A.25) and the $SGDC(r)$ (Equation 1) are highly correlated with the emergence of local salient events (see Figures B.9C,G), they fail to reproduce the topography of co-activations associated with the observed neuronal avalanches (compare Figures 6A,B with Figures B.9A,B,E,F and see the regressions in Figures B.9D,H). Of note, the $SGDC(r)$ measure essentially quantifies the presence of above-threshold bursts mainly associated with SGDC in the alpha band, whereas kurtosis assesses the presence of both oscillatory and non-oscillatory above-threshold fluctuations (outliers in the tails of the distribution of amplitude values). To account for both the burstiness and cross-regional bursts synchronization we used the pairwise SGDC measure (pSGDC). The $pSGDC(r_1, r_2)$ is defined as a factor quantifying the cross-regional correlation between the group delays across the frequency values, weighted by the average $SGDC(r)$ of each pair of signals r_1 and r_2 (see Equation 3 in Methods and Equations A.23 and A.24 in Appendix A.3). Figures 6D-F show that the profile of co-bursting across brain regions, as quantified by the $pSGDC(r_1, r_2)$ measure, significantly correlates with the observed co-activations topography and also generates statistics that are lost in the A- and B-surrogates. In our MEG dataset we found that, similarly to the pSGDC measure, the cokurtosis, as defined in the Equation A.26, also correlates with the observed co-activations topography and generates statistics that are lost in the A- and B-surrogates (see Figures 6G-I). Linear correlations: Co-activations vs pSGDC, $r = 0.390$, $P < 0.001$ (Figure 6F). Co-activations vs Cokurtosis, $r = 0.388$, $P < 0.001$ (Figure 6I). Co-activations vs Pairwise Pearson's correlation, $r = 0.252$, $P = 0.021$ (data not shown). The statistical significance of these linear correlations was assessed by using the Student's t distributions of the two-tailed hypothesis test under the null hypothesis that the correlation is zero. Of note, the pSGDC measure quantifies the co-occurrence of above-threshold bursts mainly associated with SGDC in the alpha band, whereas cokurtosis assesses the presence of both oscillatory and non-oscillatory co-burstiness across brain regions. Importantly, the analysis proposed here based on the $SGDC(r)$, $SGDC(\omega)$ and $pSGDC(r_1, r_2)$ measures, admits relevant mechanistic interpretations linking the Fourier oscillatory constituents of the brain activity and neuronal avalanches. Specifically, the avalanches co-activation pattern reproduced by the pSGDC measure (see Figures 6A-F) can be mechanistically segregated in two components: 1) the results associated with the $SGDC(r)$ measure (Figures B.9E-H) supporting the emergence of local above-threshold fluctuations via SGDC mainly in the alpha band,

692 and 2) the results associated with the $SGDC(\omega)$ measure (Figure B.10F) supporting
 693 the co-occurrence of above-threshold alpha bursts across brain regions
 694 (i.e., transient cross-regional coherence around the alpha band). The component
 695 1 can be interpreted as an entraining mechanism producing transient synchronizations
 696 of the oscillatory activity of neuronal populations around specific frequency bands (local cross-frequency synchronization), whereas the component
 697 2 can be associated with a long-range interaction via transient cross-regional
 698 coherence in narrowband oscillations.
 699

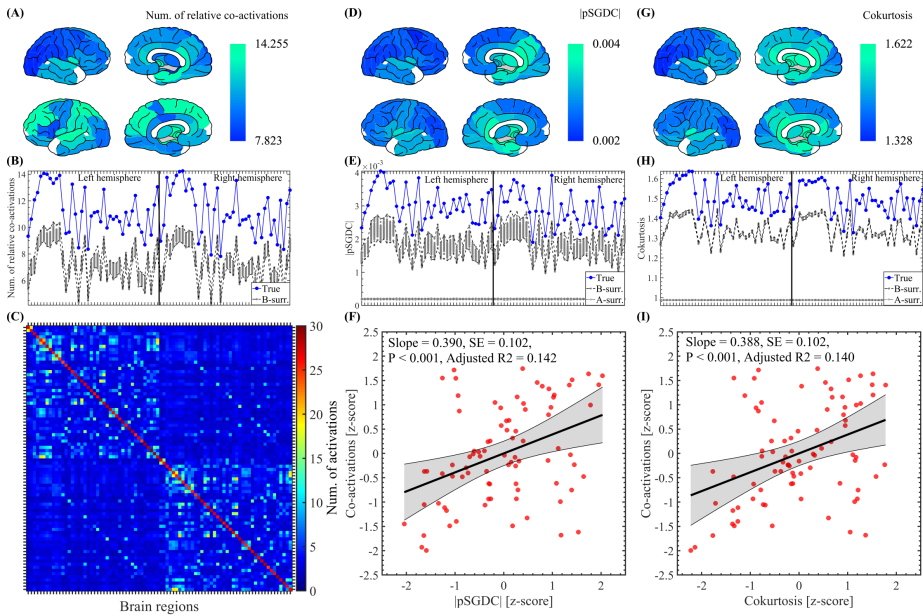


Figure 6: Co-activation pattern of brain avalanches compared against pSGDC and cokurtosis measures computed on whole time series of the brain regions taken in pairs. (A) Brain topographies corresponding to the co-activation profile shown in panel B (blue markers). (B) Spatial profile showing the number of relative co-activations (mean value across the 47 participants), i.e., the accumulated number of activations in each row of the co-activation matrix relative to the total number of activations in each brain region (diagonal of the co-activation matrix). (C) Co-activation matrix averaged across the 47 participants (see Methods). (D-E) Same as in A-B for the pSGDC measure. (F) Scatter plot showing the correlation between the co-activation and pSGDC spatial profiles shown in panels B and E, respectively. Number of samples (red circles) = Number of brain regions = 84. The thick black line and black shaded error bars represent the linear regression and the 95% confidence interval, respectively. The reported P value for the statistical significance of the linear regression was assessed using Student's t distributions of the two-tailed hypothesis test under the null hypothesis that the correlation is zero. (G-I) Same as in D-F for the cokurtosis measure.

700 4. DISCUSSION

701 Frequency-domain representation of brain signals, via Fourier transforms
 702 (e.g., DFT), have been extensively used for decades in many neuroscience fields

703 to analyze the neural activity across several spatiotemporal scales. Regardless of
704 the functional significance of neural oscillations, if any, the Fourier basis func-
705 tions provide an arguably good characterization of the rhythmic components
706 observed in the brain activity. In this study, we used the complex baseband
707 representation of signals, based on the Fourier theory, to analytically define the
708 spectral group delay consistency (SGDC) as a novel conceptualization linking
709 brain avalanches with the signals' spectral content. Importantly, the SGDC
710 framework allowed us to provide a unifying rationale for the emergence of local
711 salient events and neuronal avalanches from the Fourier oscillatory constituents
712 of the brain activity. First, the analytical arguments described in Appendix A.2
713 point out that in order to observe realistic local above-threshold fluctuations, the
714 spectral components constituting the brain signals must disclose a certain degree
715 of cross-frequency coherence as assessed by the $SGDC(r)$ measure (see Figures
716 4A-C, 4D-F, B.6, B.7, A.1 and A.2). Second, we analytically showed that A-
717 and B-surrogates failed to reproduce realistic neuronal avalanches mainly be-
718 cause the phase randomization reduces the SGDC across both frequency bands
719 and brain regions which impairs a) the burstiness of each signal (occurrence
720 of above-threshold fluctuations) and b) the synchronization of above-threshold
721 fluctuations across brain regions, respectively (see Section 3.5 and Appendix
722 A.4). Third, the spectral signature in the alpha band disclosed by the av-
723 eraged ASM of cluster 2 avalanches constitutes relevant evidence linking the
724 observed brain avalanches with narrowband oscillations. Importantly, this fea-
725 ture associated with the synchronization of above-threshold alpha bursts across
726 brain regions can be explained in terms of the SGDC mechanism through the
727 $SGDC(\omega)$ measure (see Figures B.10F,G and Sections 3.5 and 3.6). Fourth, the
728 SGDC conceptualization allowed us, via the $pSGDC(r_1, r_2)$ measure, to explain
729 both the co-activation pattern of brain avalanches and cokurtosis in terms of the
730 coherence of the signals' spectral content, therefore, advancing our understand-
731 ing of the mechanisms of long-range communication. The empiric, modeling
732 and analytical results presented in this work guided us to identify the essen-
733 tial building blocks underlying the emergence of realistic neuronal avalanches
734 as observed in our MEG dataset, which can be summarized as follows:

- 735 1 Spectral group delay consistency. This feature explains the emergence, in a
736 single brain region (i.e., locally), of transient above-threshold fluctuations as-
737 sociated with an specific frequency band (e.g., alpha bursts). The SGDC (e.g.,
738 bounded phase differences across spectral components associated with the al-
739 pha peak) can be interpreted as an entraining mechanism producing transient
740 synchronizations of the oscillatory activity of neuronal populations around
741 specific frequency bands. We note that bounded phase differences across
742 spectral components might be produced by neuronal populations that are
743 communicating locally, under the communication-through-coherence (CTC)
744 hypothesis.
- 745 2 Transient cross-regional coherent alpha oscillations. This feature explains the
746 transient synchronization of the above-threshold alpha bursts across brain
747 regions, giving rise to the neuronal avalanches producing the alpha spec-

748 tral signature in the ASM (i.e., avalanche cluster 2). This type of neuronal
749 avalanches can be putatively associated with a long-range interaction mech-
750 anism through specific narrowband oscillations taking place in a transient
751 manner (i.e., transient CTC).

752 3 Broadband $1/f$ activity. This feature explains the emergence of non-oscillatory
753 above-threshold fluctuations occurring in an aperiodic manner, mainly as-
754 sociated with the short-lived avalanches with no characteristic spectral sig-
755 nificance in the ASM (i.e., avalanche cluster 1). The close relationship be-
756 tween avalanche cluster 1 and the $1/f$ spectral features implies that this type
757 of avalanches could play a more local role linked to either local excitation-
758 inhibition balance or to critical dynamics [7].

759 Linking the presence of neuronal avalanches to the group delay consistency
760 across the Fourier oscillatory components of the brain activity is a relevant re-
761 sult of this study implying that avalanches might mediate interactions across
762 both frequency bands and brain regions as discussed above. In this regard, the
763 CTC hypothesis posits that neural communication is facilitated by the presence
764 of synchronized (steady) oscillations across brain regions. Our results extend the
765 CTC hypothesis by showing that long-range interaction through specific narrow-
766 band oscillations may take place in a transient manner via neuronal avalanches
767 (i.e., transient CTC). Indeed, the results presented in the Figure B.10 suggest
768 that the large-scale spreading of alpha bursts occurs mainly via brain avalanches.
769 As a result, this evidence suggests that transient cross-regional coherence asso-
770 ciated with the occurrence of neuronal avalanches disclosing the spectral signa-
771 ture in the alpha band (i.e., avalanche cluster 2), may play a functional role as a
772 long-range interaction mechanism in the resting human brain. One of the main
773 limitations of this study is related to the uncertain capability of our dataset to
774 accurately identify deep brain sources along the cortical surface, mainly due to
775 the ill-posed nature of the source-reconstructed MEG data. In order to address
776 this issue, we re-computed the analysis of avalanches presented in this work, but
777 this time excluding the deep sources. It was found that all the conclusions and,
778 in particular, all the characteristics of the observed neuronal avalanches remain
779 essentially unaltered when the deep sources are excluded from the avalanche
780 analysis (See Figures B.11 and B.12 in Section Appendix B.3).

781 5. CONCLUSION

782 In this work we provided a detailed analytical description of the mechanisms
783 underlying the emergence of neuronal avalanches from narrowband oscillations
784 and broadband arrhythmic activity co-existing in the human brain. The pro-
785 posed analytical arguments were tested and confirmed using local and large-scale
786 models together with experimental data (MEG recordings obtained in healthy
787 subjects during closed-eyes resting state). We also discussed the evidence in
788 connection with the large-scale spreading of alpha bursts associated with the
789 occurrence of neuronal avalanches, as a long-range interaction mechanism in
790 the resting human brain.

791 **ACKNOWLEDGEMENTS**

792 **REFERENCES**

- 793 [1] B. J. He, Scale-free brain activity: past, present, and future, *Trends Cogn
794 Sci* 18 (9) (2014) 480–487. [doi:10.1016/j.tics.2014.04.003](https://doi.org/10.1016/j.tics.2014.04.003).
- 795 [2] György Buzsáki, *Rhythms of the Brain*, Oxford University Press, 2006.
- 796 [3] H. Berger, Über das Elektrenkephalogramm des Menschen, *Archiv F Psy-
797 chiatrie* 87 (1929) 527–570. [doi:10.1007/BF01797193](https://doi.org/10.1007/BF01797193).
- 798 [4] E. D. Adrian, B. H. C. Matthews, The Berger rhythm: Potential changes
799 from the occipital lobes in man, *Brain* 57 (1934) 355–385. [doi:10.1093/
800 brain/57.4.355](https://doi.org/10.1093/brain/57.4.355).
- 801 [5] S. Palva, P. J. M., New vistas for alpha-frequency band oscillations, *Trends
802 in Neurosciences* 30 (2007) 150–158. [doi:10.1016/j.tins.2007.02.001](https://doi.org/10.1016/j.tins.2007.02.001).
- 803 [6] C. A. Bosman, C. S. Lansink, C. M. Pennartz, Functions of gamma-band
804 synchronization in cognition: from single circuits to functional diversity
805 across cortical and subcortical systems, *Eur J Neurosci* 39 (2014) 1982–
806 1999. [doi:10.1111/ejn.12606](https://doi.org/10.1111/ejn.12606).
- 807 [7] A. Nanda, G. W. Johnson, Y. Mu, M. B. Ahrens, C. Chang, D. J. Englot,
808 M. Breakspear, M. Rubinov, Time-resolved correlation of distributed brain
809 activity tracks E-I balance and accounts for diverse scale-free phenomena,
810 *Cell Rep* 42 (112254). [doi:10.1016/j.celrep.2023.112254](https://doi.org/10.1016/j.celrep.2023.112254).
- 811 [8] M. Gerster, G. Waterstraat, V. Litvak, K. Lehnertz, A. Schnitzler,
812 E. Florin, G. Curio, V. Nikulin, Separating Neural Oscillations from Ap-
813 eriodic 1/f Activity: Challenges and Recommendations, *Neuroinform* 20
814 (2022) 991–1012. [doi:10.1007/s12021-022-09581-8](https://doi.org/10.1007/s12021-022-09581-8).
- 815 [9] C. Keitel, M. Ruzzoli, L. Dugué, N. A. Busch, C. S. Y. Benwell, Rhythms
816 in cognition: The evidence revisited, *Eur J Neurosci* 55 (2022) 2991–3009.
817 [doi:10.1111/ejn.15740](https://doi.org/10.1111/ejn.15740).
- 818 [10] J. M. Beggs, D. Plenz, Neuronal avalanches in neocortical circuits, *J
819 Neurosci* 23 (2003) 11167–11177. [doi:10.1523/JNEUROSCI.23-35-11167.
820 2003](https://doi.org/10.1523/JNEUROSCI.23-35-11167.2003).
- 821 [11] J. M. Beggs, D. Plenz, Neuronal avalanches are diverse and precise activity
822 patterns that are stable for many hours in cortical slice cultures, *J Neurosci*
823 24 (2004) 5216–5229. [doi:10.1523/JNEUROSCI.0540-04.2004](https://doi.org/10.1523/JNEUROSCI.0540-04.2004).
- 824 [12] J. M. Palva, A. Zhigalov, J. Hirvonen, O. Korhonen, K. Linkenkaer-Hansen,
825 S. Palva, Neuronal long-range temporal correlations and avalanche dynam-
826 ics are correlated with behavioral scaling laws, *Proc Natl Acad Sci U S A*
827 110 (2013) 3585–3590. [doi:10.1073/pnas.1216855110](https://doi.org/10.1073/pnas.1216855110).

- 828 [13] G. M. Duma, A. Danieli, G. Mento, V. Vitale, R. S. Opiplari, V. Jirsa,
829 P. Bonanni, P. Sorrentino, Altered spreading of neuronal avalanches in
830 temporal lobe epilepsy relates to cognitive performance: A resting-state
831 hdEEG study, *Epilepsia* 64 (2023) 1278–1288. doi:[10.1111/epi.17551](https://doi.org/10.1111/epi.17551).
- 832 [14] O. Shriki, J. Alstott, F. Carver, T. Holroyd, R. N. Henson, M. L. Smith,
833 R. Coppola, E. Bullmore, D. Plenz, Neuronal avalanches in the resting
834 MEG of the human brain, *J Neurosci* 33 (2013) 7079–7090. doi:[10.1523/JNEUROSCI.4286-12.2013](https://doi.org/10.1523/JNEUROSCI.4286-12.2013).
- 836 [15] V. Priesemann, M. Valderrama, M. Wibral, M. Le Van Quyen, Neuronal
837 avalanches differ from wakefulness to deep sleep-evidence from intracranial
838 depth recordings in humans, *PLoS Comput Biol* 9 (e1002985). doi:[10.1371/journal.pcbi.1002985](https://doi.org/10.1371/journal.pcbi.1002985).
- 840 [16] A. Zhigalov, G. Arnulfo, L. Nobili, S. Palva, J. M. Palva, Relationship of
841 fast- and slow-timescale neuronal dynamics in human MEG and SEEG, *J
842 Neurosci* 35 (2015) 5385–5396. doi:[10.1523/JNEUROSCI.4880-14.2015](https://doi.org/10.1523/JNEUROSCI.4880-14.2015).
- 843 [17] E. Tagliazucchi, P. Balenzuela, D. Fraiman, D. R. Chialvo, Criticality in
844 large-scale brain fMRI dynamics unveiled by a novel point process analysis,
845 *Front Physiol* 3. doi:[10.3389/fphys.2012.00015](https://doi.org/10.3389/fphys.2012.00015).
- 846 [18] M. Yaghoubi, T. de Graaf, J. G. Orlandi, F. Girotto, M. A. Colicos, J. Davidsen, Neuronal avalanche dynamics indicates different uni-
847 versality classes in neuronal cultures, *Sci Rep* 8 (3417). doi:[10.1038/s41598-018-21730-1](https://doi.org/10.1038/s41598-018-21730-1).
- 850 [19] Z. Bowen, D. E. Winkowski, S. Seshadri, D. Plenz, P. O. Kanold, Neuronal
851 Avalanches in Input and Associative Layers of Auditory Cortex, *Front Syst
852 Neurosci* 13. doi:[10.3389/fnsys.2019.00045](https://doi.org/10.3389/fnsys.2019.00045).
- 853 [20] W. L. Shew, H. Yang, S. Yu, R. Roy, D. Plenz, Information capacity
854 and transmission are maximized in balanced cortical networks with neu-
855 ronal avalanches, *J Neurosci* 31 (2011) 55–63. doi:[10.1523/JNEUROSCI.4637-10.2011](https://doi.org/10.1523/JNEUROSCI.4637-10.2011).
- 857 [21] W. L. Shew, D. Plenz, The functional benefits of criticality in the cortex,
858 *Neuroscientist* 19 (2013) 88–100. doi:[10.1177/1073858412445487](https://doi.org/10.1177/1073858412445487).
- 859 [22] O. Kinouchi, M. Copelli, Optimal dynamical range of excitable networks
860 at criticality, *Nature Phys* 2 (2006) 348–351. doi:[10.1038/nphys289](https://doi.org/10.1038/nphys289).
- 861 [23] D. B. Larremore, W. L. Shew, J. G. Restrepo, Predicting criticality and
862 dynamic range in complex networks: effects of topology, *Phys Rev Lett*
863 106 (058101). doi:[10.1103/PhysRevLett.106.058101](https://doi.org/10.1103/PhysRevLett.106.058101).
- 864 [24] E. Tognoli, J. A. Kelso, The metastable brain, *Neuron* 81 (2014) 35–48.
865 doi:[10.1016/j.neuron.2013.12.022](https://doi.org/10.1016/j.neuron.2013.12.022).

- 866 [25] P. Sorrentino, R. Rucco, F. Baselice, R. De Micco, A. Tessitore, A. Hille-
867 brand, L. Mandolesi, M. Breakspear, L. Gollo, G. Sorrentino, Flexible brain
868 dynamics underpins complex behaviours as observed in Parkinson's disease,
869 *Sci Rep* 11 (4051). doi:10.1038/s41598-021-83425-4.
- 870 [26] P. Sorrentino, S. Petkoski, M. Sparaco, E. Troisi Lopez, E. Signoriello,
871 F. Baselice, S. Bonavita, M. A. Pirozzi, M. Quarantelli, G. Sorrentino,
872 V. Jirsa, Whole-Brain Propagation Delays in Multiple Sclerosis, a Com-
873 bined Tractography-Magnetoencephalography Study, *J Neurosci* 42 (47)
874 (2022) 8807–8816. doi:10.1523/JNEUROSCI.0938-22.2022.
- 875 [27] P. Moretti, M. A. Muñoz, Griffiths phases and the stretching of criticality
876 in brain networks, *Nat Commun* 4 (2521). doi:10.1038/ncomms3521.
- 877 [28] D. Plenz, Criticality in cortex: neuronal avalanches and coherence po-
878 tentials, In: *Criticality in neural systems* (2014) 5–42doi:10.1002/
879 9783527651009.ch2.
- 880 [29] O. Arviv, A. Goldstein, O. Shriki, Neuronal avalanches and time-frequency
881 representations in stimulus-evoked activity, *Sci Rep* 16 (13319). doi:10.
882 1038/s41598-019-49788-5.
- 883 [30] S. R. Miller, S. Yu, D. Plenz, The scale-invariant, temporal profile of neu-
884 ronal avalanches in relation to cortical γ -oscillations, *Sci Rep* 9 (16403).
885 doi:10.1038/s41598-019-52326-y.
- 886 [31] P. Sorrentino, C. Seguin, R. Rucco, M. Liparoti, E. Troisi Lopez,
887 S. Bonavita, M. Quarantelli, G. Sorrentino, V. Jirsa, A. Zalesky, The
888 structural connectome constrains fast brain dynamics, *eLife* 10. doi:
889 10.7554/eLife.67400.
- 890 [32] S. Rombetto, C. Granata, A. Vettoliere, M. Russo, Multichannel system
891 based on a high sensitivity superconductive sensor for magnetoencephalog-
892 raphy, *Sensors* 14 (2014) 12114–12126. doi:10.3390/s140712114.
- 893 [33] D. Dellavale, F. Bonini, F. Pizzo, J. Makhalova, F. Wendling, J. M.
894 Badier, F. Bartolomei, C. G. Bénar, Spontaneous fast-ultradian dynamics
895 of polymorphic interictal events in drug-resistant focal epilepsy, *Epilepsia*
896 64 (2023) 2027–2043. doi:10.1111/epi.17655.
- 897 [34] V. D. Blondel, J.-L. Guillaume, R. Lambiotte, E. Lefebvre, Fast unfolding
898 of communities in large networks, *J Stat Mech* 2008 (P10008). doi:10.
899 1088/1742-5468/2008/10/P10008.
- 900 [35] M. Rubinov, O. Sporns, Weight-conserving characterization of complex
901 functional brain networks, *Neuroimage* 56. doi:10.1016/j.neuroimage.
902 2011.03.069.

- 903 [36] Shafiei, G. and Zeighami, Y. and Clark, C. A. and Coull, J. T. and Nagano-
904 Saito, A. and Leyton, M. and Dagher, A. and Mišić, B., Dopamine Signaling
905 Modulates the Stability and Integration of Intrinsic Brain Networks, *Cereb Cortex* 29 (2019) 397–409. doi:[10.1093/cercor/bhy264](https://doi.org/10.1093/cercor/bhy264).
- 906
- 907 [37] A. Lancichinetti, S. Fortunato, Consensus clustering in complex networks,
908 *Sci Rep* 2 (336). doi:[10.1038/srep00336](https://doi.org/10.1038/srep00336).
- 909 [38] D. S. Bassett, M. A. Porter, N. F. Wymbs, S. T. Grafton, J. M. Carlson,
910 P. J. Mucha, Robust detection of dynamic community structure in
911 networks, *Chaos* 23 (013142). doi:[10.1063/1.4790830](https://doi.org/10.1063/1.4790830).
- 912 [39] B. R. F., Community detection in network neuroscience, arXiv
913 arXiv:2011.06723. doi:[10.48550/arXiv.2011.06723](https://doi.org/10.48550/arXiv.2011.06723).
- 914 [40] R. Bracewell, *The Fourier Transform And Its Applications*, 3rd Edition,
915 McGraw-Hill, 2000.
- 916 [41] M. X. Cohen, *Analyzing neural time series data : theory and practice*, 1st
917 Edition, MIT Press, 2014.
- 918 [42] P. Fries, A mechanism for cognitive dynamics: neuronal communication
919 through neuronal coherence, *Trends in Cognitive Sciences* 9 (2005) 474–
920 480. doi:[10.1016/j.tics.2005.08.011](https://doi.org/10.1016/j.tics.2005.08.011).
- 921 [43] R. Hindriks, P. K. B. Tewarie, Dissociation between phase and power cor-
922 relation networks in the human brain is driven by co-occurrent bursts,
923 *Communications Biology* 6 (286). doi:[10.1038/s42003-023-04648-x](https://doi.org/10.1038/s42003-023-04648-x).
- 924 [44] A. V. Oppenheim, R. W. Schafer, J. R. Buck, *Discrete-Time Signal Pro-*
925 *cessing*, 2nd Edition, Prentice Hall, 1998.
- 926 [45] J. G. Proakis, *Digital Communications*, 4th Edition, McGraw-Hill, 2000.
- 927 [46] S. Haykin, *Communication Systems*, 4th Edition, John Wiley & Sons, 2000.
- 928 [47] P. Berens, CircStat: A MATLAB Toolbox for Circular Statistics, *Journal*
929 *of Statistical Software* 31 (10) (2009) 1–21. doi:[10.18637/jss.v031.i10](https://doi.org/10.18637/jss.v031.i10).
- 930 [48] P. Tass, M. G. Rosenblum, J. Weule, J. Kurths, A. Pikovsky, J. Volkmann,
931 A. Schnitzler, H.-J. Freund, Detection of $n : m$ Phase Locking from Noisy
932 Data: Application to Magnetoencephalography, *Physical Review Letters*
933 81 (0) (1998) 3291–3294. doi:[10.1103/PhysRevLett.81.3291](https://doi.org/10.1103/PhysRevLett.81.3291).
- 934 [49] J. P. Lachaux, E. Rodriguez, J. Martinerie, F. J. Varela, Measuring phase
935 synchrony in brain signals, *Hum Brain Mapp* 8 (1999) 3194–208. doi:
936 [10.1002/\(SICI\)1097-0193\(1999\)8:4<194::AID-HBM4>3.0.CO;2-C](https://doi.org/10.1002/(SICI)1097-0193(1999)8:4<194::AID-HBM4>3.0.CO;2-C).

1 Appendix A. Supplementary methods

2 Appendix A.1. Preservation of the Pearson's cross-correlation in the B-surrogates

3

4 Let us start by considering the circular cross-correlation $R_{xy}(t')$ between the
 5 time series $x(t)$ and $y(t)$ representing the activities of two brain regions [44, pp.
 6 571, 746],

$$R_{xy}(t') = \sum_{t=0}^{N_s-1} x^*(t - t')_{\text{mod } N_s} y(t) \quad (\text{A.1})$$

7 where $(x(t), y(t)) \in \mathbb{R}$ are finite-length discrete time series having N_s time
 8 samples satisfying $(x(t) = 0, y(t) = 0) \forall 0 > t > N_s - 1$, being $t \in \mathbb{Z}$ the
 9 discrete time index. By applying the Discrete Fourier Transform (DFT) $\mathfrak{F}\{\cdot\}$
 10 on both sides of eq. A.1 we obtain [44, pp. 575, 746],

$$\begin{aligned} S_{xy}(\omega) &= \mathfrak{F}\{R_{xy}(t')\} \\ &= \mathfrak{F}\{x(t)\}^* \mathfrak{F}\{y(t)\} = A_x(\omega)e^{-i\phi_x(\omega)} A_y(\omega)e^{i\phi_y(\omega)} \end{aligned} \quad (\text{A.2})$$

11 where $A_x(\omega)$, $\phi_x(\omega)$ and $A_y(\omega)$, $\phi_y(\omega)$ are the magnitude and phase angle of
 12 the DFT spectrum corresponding to the signals $x(t)$ and $y(t)$, respectively. The
 13 computation of surrogate time series involves the addition of random phases
 14 $\theta(\omega)$ to the corresponding DFT spectra as follows,

$$\begin{aligned} S_{xy}^s(\omega) &= A_x(\omega)e^{-i(\phi_x(\omega)+\theta_x(\omega))} A_y(\omega)e^{i(\phi_y(\omega)+\theta_y(\omega))} \\ &= A_x(\omega)e^{-i\phi_x(\omega)} A_y(\omega)e^{i\phi_y(\omega)} e^{i(\theta_y(\omega)-\theta_x(\omega))} \end{aligned} \quad (\text{A.3})$$

15 In the A.3, $S_{xy}^s(\omega)$ is the DFT of the circular cross-correlation associated with
 16 the surrogated time series $x^s(t) = \mathfrak{F}^{-1}\{A_x(\omega)e^{-i(\phi_x(\omega)+\theta_x(\omega))}\}$ and $y^s(t) =$
 17 $\mathfrak{F}^{-1}\{A_y(\omega)e^{-i(\phi_y(\omega)+\theta_y(\omega))}\}$, where $\mathfrak{F}^{-1}\{\cdot\}$ stands for the inverse DFT. In the
 18 particular case of the B-surrogates we add the same random phase-shift in all
 19 the brain regions, that is, $\theta_x(\omega) = \theta_y(\omega)$ producing $e^{i(\theta_y(\omega)-\theta_x(\omega))} = 1$ in the eq.
 20 A.3. Under this condition, the eqs. A.2 and A.3 becomes equivalent which in
 21 turn implies the equivalence between the circular cross-correlations associated
 22 with the true data and the B-surrogate,

$$\begin{aligned} S_{xy}(\omega) = S_{xy}^s(\omega) &\implies \mathfrak{F}\{R_{xy}(t')\} = \mathfrak{F}\{R_{xy}^s(t')\} \\ &\implies R_{xy}(t') = R_{xy}^s(t') \end{aligned}$$

23 Appendix A.2. Oscillatory mechanisms underlying the emergence of local above-threshold fluctuations

24 In this section we provide a detailed description of the mechanism underlying
 25 the emergence of local above-threshold fluctuations from the Fourier oscillatory
 26 constituents of the brain activity. Our analysis start by projecting the brain
 27 signal of interest $x(t)$ onto the Fourier basis functions using the Discrete Fourier
 28 Transform (DFT) equations [44, Chapters 8 and 10]. In doing so we are assuming
 29 that $x(t)$ satisfies certain conditions so the resulting spectral estimates exist

and are meaningful. Specifically, by considering finite-length time series constituted by N_s time samples, the existence of the DFT representation requires that $x(t)$ is bounded ($|x(t)| < M \in \mathbb{R} \forall 0 > t > N_s - 1$). Besides, the analyzed brain activity are in general nonstationary, that is, the time series $x(t)$ can be represented as a sum of sinusoidal components with time-varying amplitudes, frequencies, or phases. In this regard, we consider a small enough number of time samples N_s such that the spectral characteristics of the signal $x(t)$ can be assumed stationary during the analyzed time window. Thus, by considering $x(t) \in \mathbb{R}$ being a finite-length discrete time series having an even number of time samples N_s and $x(t) = 0 \forall 0 > t > N_s - 1$, where $t \in \mathbb{Z}$ is the discrete time index. The analysis equation corresponding to the Discrete Fourier Transform (DFT) of $x(t)$ can be written as follows [44, p. 561, Eq. (8.67)],

$$X(k) = \sum_{t=0}^{N_s-1} x(t)e^{-i\omega_0 kt} : \omega_0 = \frac{2\pi}{N_s} \quad (\text{A.4})$$

where $k \in \mathbb{Z}$ is the discrete frequency index, in general producing complex Fourier coefficients $X(k) \in \mathbb{C}$ and $X(k) = 0 \forall 0 > k > N_s - 1$. Then, the synthesis equation associated with the inverse DFT (iDFT) is [44, p. 561, Eq. (8.68)],

$$x(t) = \frac{1}{N_s} \sum_{k=0}^{N_s-1} X(k)e^{i\omega_0 kt} \quad (\text{A.5})$$

Taking into account that $X(k) = |X(k)|e^{i\phi(k)} \in \mathbb{C}$, the eq. A.5 can be rewritten as,

$$x(t) = \frac{1}{N_s} \sum_{k=0}^{N_s-1} |X(k)|e^{i(\omega_0 kt + \phi(k))} \quad (\text{A.6})$$

The core of the proposed conceptualization is to note that the eq. A.6 can be expressed as a sum of (non-overlapping) pairwise adjacent spectral components as follows,

$$\begin{aligned} x(t) &= \frac{1}{N_s} \sum_{k=0}^{N_s/2-1} |X(2k)|e^{i(\omega_0 2kt + \phi(2k))} \\ &\quad + |X(2k+1)|e^{i(\omega_0 (2k+1)t + \phi(2k+1))} \\ x(t) &= \frac{1}{N_s} \sum_{k=0}^{N_s/2-1} \left(|X(2k)|e^{i\phi(2k)} + |X(2k+1)|e^{i(\omega_0 t + \phi(2k+1))} \right) e^{i\omega_0 2kt} \end{aligned}$$

By defining the forward phase difference as $\Delta\phi(2k) = \phi(2k+1) - \phi(2k)$, and substituting $\phi(2k+1) = \phi(2k) + \Delta\phi(2k)$ in the previous equation we have,

$$\begin{aligned} x(t) &= \frac{1}{N_s} \sum_{k=0}^{N_s/2-1} \left(|X(2k)|e^{-i(\frac{\omega_0}{2}t + \frac{\Delta\phi(2k)}{2})} \right. \\ &\quad \left. + |X(2k+1)|e^{i(\frac{\omega_0}{2}t + \frac{\Delta\phi(2k)}{2})} \right) e^{i\frac{\omega_0}{2}t} e^{i(\phi(2k) + \frac{\Delta\phi(2k)}{2})} e^{i\omega_0 2kt} \end{aligned}$$

$$\begin{aligned} x(t) &= \frac{1}{N_s} \sum_{k=0}^{N_s/2-1} \left(|X(2k)| e^{-i(\frac{\omega_0}{2}t + \frac{\Delta\phi(2k)}{2})} \right. \\ &\quad \left. + |X(2k+1)| e^{i(\frac{\omega_0}{2}t + \frac{\Delta\phi(2k)}{2})} \right) e^{i(\frac{\omega_0}{2}(4k+1)t + \phi(2k) + \frac{\Delta\phi(2k)}{2})} \end{aligned}$$

55 Then, by introducing in the previous equation the forward frequency difference
 56 $\Delta\omega = \omega_0(k+1) - \omega_0 k = \omega_0$, it results,

$$\begin{aligned} x(t) &= \frac{1}{N_s} \sum_{k=0}^{N_s/2-1} \left(|X(2k)| e^{-i(\frac{\Delta\omega}{2}t + \frac{\Delta\phi(2k)}{2})} \right. \\ &\quad \left. + |X(2k+1)| e^{i(\frac{\Delta\omega}{2}t + \frac{\Delta\phi(2k)}{2})} \right) e^{i(\frac{\Delta\omega}{2}(4k+1)t + \phi(2k) + \frac{\Delta\phi(2k)}{2})} \end{aligned}$$

57 Taking out $\Delta\omega/2$ as a common factor we have,

$$\begin{aligned} x(t) &= \frac{1}{N_s} \sum_{k=0}^{N_s/2-1} \left(|X(2k)| e^{-i\frac{\Delta\omega}{2}(t + \frac{\Delta\phi(2k)}{\Delta\omega})} \right. \\ &\quad \left. + |X(2k+1)| e^{i\frac{\Delta\omega}{2}(t + \frac{\Delta\phi(2k)}{\Delta\omega})} \right) e^{i(\frac{\Delta\omega}{2}(4k+1)t + \phi(2k) + \frac{\Delta\phi(2k)}{2})} \end{aligned}$$

58 The rate of change of the phase with the frequency is associated with the group
 59 delay defined as $\tau(k) = -\Delta\phi(k)/\Delta\omega$. Using this definition, the previous equa-
 60 tion can be written as,

$$\begin{aligned} x(t) &= \frac{1}{N_s} \sum_{k=0}^{N_s/2-1} \underbrace{\left(|X(2k)| e^{-i\frac{\Delta\omega}{2}(t - \tau(2k))} + |X(2k+1)| e^{i\frac{\Delta\omega}{2}(t - \tau(2k))} \right)}_{\text{Complex envelope (sidebands)}} \\ &\quad \times \underbrace{e^{i(\frac{\Delta\omega}{2}(4k+1)t + \phi(2k) + \frac{\Delta\phi(2k)}{2})}}_{\text{Complex carrier}} \end{aligned} \tag{A.7}$$

61 It is essential to note that in eq. A.7, each (non-overlapping) pair of adjacent
 62 spectral components $X(2k), X(2k+1)$ can be interpreted as the sidebands of an
 63 amplitude modulated carrier at $(4k+1)\Delta\omega/2$. Importantly, the frequency of the
 64 carrier $(4k+1)\Delta\omega/2$ is a function of the frequency index k , that is, it depends on
 65 the particular pair of spectral components under consideration ($X(2k), X(2k +$
 66 $1)$). However, the frequency of the modulating component is the same for all
 67 the pair of spectral components involved in eq. A.7, i.e., it is independent of
 68 the frequency index k and only determined by the frequency resolution of the
 69 DFT as $\Delta\omega/2 = \omega_0/2$ (i.e., half the separation between the two sidebands).
 70 Another important characteristic of the representation given by the eq. A.7 is
 71 that the frequencies associated with the complex envelopes ($\Delta\omega/2$) and with the
 72 complex carrier ($(4k+1)\Delta\omega/2$) satisfy the condition $\Delta\omega/2 \leq (4k+1)\Delta\omega/2$. In
 73 the telecom theory, a spectral profile satisfying these characteristics is known as

74 the complex baseband representation of a band-limited signal (e.g., amplitude
 75 modulated signal) [44, Chapter 11.4.2, p. 796; 45, Chapter 4.1, p. 152; 46,
 76 Chapter A2.4, p. 725]. Accordingly, we refer to the eq. A.7 as the inverse
 77 DFT based on the pairwise complex baseband representation of $x(t)$. In line
 78 with this, the eq. A.7 can be rewritten as a summation of amplitude modulated
 79 signals corresponding to each pair of adjacent spectral components as follows,

$$x(t) = \frac{1}{N_s} \sum_{k=0}^{N_s/2-1} x_{k+}(t) \quad (\text{A.8})$$

$$x_{k+}(t) = \tilde{x}_k(t - \tau(k)) e^{i(\frac{\Delta\omega}{2}(4k+1)t + \phi(2k) + \frac{\Delta\phi(2k)}{2})} \quad (\text{A.9})$$

$$\tilde{x}_k(t - \tau(k)) = |X(2k)| e^{-i\frac{\Delta\omega}{2}(t - \tau(2k))} + |X(2k+1)| e^{i\frac{\Delta\omega}{2}(t - \tau(2k))} \quad (\text{A.10})$$

80 In the eq. A.8, $x_{k+}(t)$ is the discrete time analytic signal (a.k.a., pre-envelope)
 81 corresponding to each amplitude modulated component constituting the orig-
 82 inal signal $x(t)$, and it is defined in eq. A.9. In the eq. A.9, $\tilde{x}_k(t - \tau(k))$
 83 is the complex envelope of each amplitude modulated component constituting
 84 the original signal $x(t)$, and it is defined in terms of the spectral components
 85 $X(k)$ in the eq. A.10. It is important to note that the alignment in time of the
 86 complex envelopes $\tilde{x}_k(t - \tau(k))$ synthesizing the original signal $x(t)$, via the eq.
 87 A.8, is determined by the group delay $\tau(k)$.

88 The eqs. A.7 - A.10 constitute a useful conceptualization linking the DFT
 89 and the complex baseband representation to explain the emergence of salient
 90 events from the Fourier oscillatory constituents of a band-limited signal. Due
 91 to the fact that the analysis proposed above is based on the DFT, in the case
 92 of $x(t) \in \mathbb{R}$ the result of the summation in eqs. A.7 and A.8 is guaranteed to
 93 be real valued. At the same time, this also restrict the validity of the anal-
 94 ysis to harmonic spectral components $\omega_0 k$ associated with the fundamental
 95 frequency $\omega_0 = 2\pi/N_s$. Now we will present the general equations valid for all
 96 the cases, that is, harmonic ($\Delta\omega(k) = \text{cte}$, $\omega(k+1)/\omega(k) \in \mathbb{Q}$), non-harmonic
 97 ($\Delta\omega(k) = \text{cte}$, $\omega(k+1)/\omega(k) \in \mathbb{R} \setminus \mathbb{Q}$) and non-uniformly spaced ($\Delta\omega(k) \neq \text{cte}$)
 98 Fourier oscillatory components. Let us consider a real valued signal $x(t) \in \mathbb{R}$
 99 resulting from the linear superposition of an even number N_s of oscillatory
 100 components of arbitrary amplitude $A(k)$, frequency $\omega(k)$ and phase $\phi(k)$.

$$x(t) = \sum_{k=0}^{N_s-1} A(k) \cos(\omega(k)t + \phi(k)) : A(k) \in \mathbb{R} \quad (\text{A.11})$$

101 Since the eq. A.11 is linear we can introduce the complex notation via the
 102 Euler's formula as follows,

$$x(t) = \Re \left\{ \sum_{k=0}^{N_s-1} A(k) e^{i(\omega(k)t + \phi(k))} \right\} \quad (\text{A.12})$$

103 In the eq. A.12, the operator $\Re \{ \cdot \}$ stands for "the real part of". By following
 104 a similar procedure applied above on the eq. A.6, the eq. A.12 can be rewritten

105 as follows,

$$\begin{aligned}
 x(t) &= \Re \left\{ \sum_{k=0}^{N_s/2-1} \left(A(2k) e^{-i(\frac{\Delta\omega(2k)}{2}t + \frac{\Delta\phi(2k)}{2})} + A(2k+1) e^{i(\frac{\Delta\omega(2k)}{2}t + \frac{\Delta\phi(2k)}{2})} \right) \right. \\
 &\quad \times \left. e^{i(\bar{\omega}(2k)t + \bar{\phi}(2k))} \right\} \\
 \Delta\phi(2k) &= \phi(2k+1) - \phi(2k) \\
 \bar{\phi}(2k) &= \frac{\phi(2k+1) + \phi(2k)}{2} = \phi(2k) + \frac{\Delta\phi(2k)}{2} \\
 \Delta\omega(2k) &= \omega(2k+1) - \omega(2k) \\
 \bar{\omega}(2k) &= \frac{\omega(2k+1) + \omega(2k)}{2} = \omega(2k) + \frac{\Delta\omega(2k)}{2}
 \end{aligned}$$

106 In this case the group delay is defined as $\tau(k) = -\frac{\Delta\phi(k)}{\Delta\omega(k)}$, thus, the previous
107 equation results,

$$\begin{aligned}
 x(t) &= \Re \left\{ \underbrace{\sum_{k=0}^{N_s/2-1} \left(A(2k) e^{-i\frac{\Delta\omega(2k)}{2}(t-\tau(2k))} + A(2k+1) e^{i\frac{\Delta\omega(2k)}{2}(t-\tau(2k))} \right)}_{\text{Complex envelope (sidebands)}} \right. \\
 &\quad \times \left. \underbrace{e^{i(\bar{\omega}(2k)t + \bar{\phi}(2k))}}_{\text{Complex carrier}} \right\} \tag{A.13}
 \end{aligned}$$

108 The eq. A.13 is the pairwise complex baseband representation of the signal $x(t)$.
109 Provided that the frequencies associated with the complex envelopes ($\Delta\omega(2k)/2$)
110 and the complex carrier ($\bar{\omega}(2k)$) satisfy the condition $\Delta\omega(2k)/2 < \bar{\omega}(2k)$, the
111 eq. A.13 can also be written as a summation of discrete time analytic signals
112 $x_{k+}(t)$ associated with amplitude modulated signals corresponding to each pair
113 of adjacent oscillatory components as follows,

$$x(t) = \Re \left\{ \sum_{k=0}^{N_s/2-1} x_{k+}(t) \right\} \tag{A.14}$$

$$x_{k+}(t) = \tilde{x}_k(t - \tau(k)) e^{i(\bar{\omega}(2k)t + \bar{\phi}(2k))} \tag{A.15}$$

$$\begin{aligned}
 \tilde{x}_k(t - \tau(k)) &= A(2k) e^{-i\frac{\Delta\omega(2k)}{2}(t-\tau(2k))} \\
 &\quad + A(2k+1) e^{i\frac{\Delta\omega(2k)}{2}(t-\tau(2k))}
 \end{aligned} \tag{A.16}$$

114 Similarly to the previous case the time alignment of the complex envelopes
115 $\tilde{x}_k(t - \tau(k))$ synthesizing the original signal $x(t)$, via the eq. A.14, is deter-
116 mined by the group delay $\tau(k)$.

117 In what follows we will use the eq. A.13 to illustrate the role of the group
118 delay in explaining the emergence of above-threshold fluctuations from the os-
119 cillatory constituents of the synthetic signal $x(t)$. As a first example, let us
120 consider a spectral profile given by set of constant-amplitude $A(k) = A = 1$

121 oscillatory components uniformly spaced $f_s \Delta\omega/(2\pi) = 1.2/\sqrt{2}$ Hz and having
 122 non-harmonic frequencies $f_s \omega(k)/(2\pi) = 0.5 + k f_s \Delta\omega/(2\pi) \in [0.5 - 5]$ Hz,
 123 where $f_s = 1024$ Hz is the sampling rate (see Figs. A.1A and A.1F). Accordingly,
 124 the eq. A.13 becomes,

$$x(t) = A \operatorname{Re} \left\{ \sum_{k=0}^{N_s/2-1} \left(e^{-i\frac{\Delta\omega}{2}(t-\tau(2k))} + e^{i\frac{\Delta\omega}{2}(t-\tau(2k))} \right) e^{i(\bar{\omega}(2k)t+\bar{\phi}(2k))} \right\}$$

125 By using the Euler's formula to rearrange the modulating factor, the previous
 126 equation results,

$$\begin{aligned} x(t) &= \frac{A}{2} \operatorname{Re} \left\{ \sum_{k=0}^{N_s/2-1} \cos \left(\frac{\Delta\omega}{2} (t - \tau(2k)) \right) e^{i(\bar{\omega}(2k)t+\bar{\phi}(2k))} \right\} \\ &= \frac{A}{2} \underbrace{\sum_{k=0}^{N_s/2-1} \cos \left(\frac{\Delta\omega}{2} (t - \tau(2k)) \right)}_{\text{Modulating component}} \underbrace{\cos \left(\bar{\omega}(2k)t + \bar{\phi}(2k) \right)}_{\text{Modulated component}} \quad (\text{A.17}) \end{aligned}$$

127 The eq. A.17 explicitly shows that any pair of adjacent oscillatory components
 128 associated with the signal $x(t)$ can be interpreted as an amplitude modulated
 129 signal with the same modulating function $\cos \left(\frac{\Delta\omega}{2} (t - \tau(2k)) \right)$. The key con-
 130 cept here is to note that, when all the oscillatory components in eq. A.17 are
 131 added together to synthesize the signal $x(t)$ in the time domain, the group
 132 delay τ will determine the time alignment of the modulating functions associ-
 133 ated with each pair of adjacent oscillatory components. As a consequence, in
 134 the case of all the spectral components $A(k) e^{i(\omega(k)t+\phi(k))}$ in eq. A.12 having
 135 constant phase produces $\Delta\phi = 0 \implies \tau = -\Delta\phi/\Delta\omega = 0$, hence, all the
 136 modulating functions $\cos \left(\frac{\Delta\omega}{2} (t - 0) \right)$ in eq. A.17 will be aligned in time (at
 137 $t = 0$) giving rise to a sinc-like function representing the maximum amplitude
 138 excursion (i.e., a salient event) that can be elicited by the set of Fourier oscil-
 139 latory components constituting the eq. A.12. In the case of all the spectral
 140 components in eq. A.12 having a phase proportional to the discrete frequency
 141 index $\phi(k) = -\tau_0 \Delta\omega k \implies \Delta\phi(k) = -\tau_0 \Delta\omega$, results in a group delay
 142 which does not dependent on the frequency $\tau(k) = -\Delta\phi(k)/\Delta\omega = \tau_0$, thus,
 143 in eq. A.12 we obtain a modulating component $\cos \left(\frac{\Delta\omega}{2} (t - \tau_0) \right)$. That is,
 144 all the modulating functions will again be aligned in time producing the same
 145 salient event given by the sinc-like function as in the previous case but this
 146 time centered at $t = \tau_0$ (i.e., a time-shift, see Figs. A.1A-E). On the other
 147 hand, in the case of the phases associated with the spectral components in eq.
 148 A.12 having a non-linear dependence with the discrete frequency index, e.g.,
 149 $\phi(k) = -\tau_0 \Delta\omega k^2 \implies \Delta\phi(k) = -\tau_0 \Delta\omega(2k+1)$, the group delay results a
 150 function of the frequency $\tau(k) = \tau_0(2k+1)$, hence, preventing the alignment in
 151 time of the modulating functions associated with each pair of adjacent spectral

152 components $\cos\left(\frac{\Delta\omega}{2}(t - \tau(k))\right)$. In this case, the signal $x(t)$ discloses sub-
153 threshold excursions of amplitude (see Figs. A.1F-J). It is worth mentioning
154 that in deriving the pairwise complex baseband representation of $x(t)$ given
155 by the eqs. A.7 and A.13, we grouped the original spectral components (eqs.
156 A.5 and A.11) in subsets of (non-overlapping) pairs adjacent in frequency. The
157 strategy of grouping the spectral components in subsets is necessary to obtain
158 a representation based on a sum of complex envelopes modulating the complex
159 carriers. Representations similar to those presented in the eqs. A.7 and A.13
160 can be obtained by defining subsets containing more than 2 non-overlapping
161 spectral components (not necessarily adjacent in frequency). However, our ap-
162 proach based on grouping adjacent spectral components in non-overlapping pairs
163 discloses the following relevant features:

- 164 1 By defining subsets of 2 spectral components, we obtain the simplest complex
165 envelopes characterized by a cos- or sin-like waveform shape (see the modu-
166 lating component in the eq. A.17 and the colored solid lines in Figs.A.1E and
167 A.2E).
- 168 2 By defining pairs of spectral components adjacent in frequency, we maximize
169 the waveform shape similarity among the resulting complex envelopes. In the
170 case of uniformly spaced spectral components ($\Delta\omega = \text{cte}$), we obtain complex
171 envelopes having the same time period $2/\Delta\omega$ (see the colored doted lines in
172 Figs.A.1E and A.2E).
- 173 3 By defining pairs of spectral components adjacent in frequency, we also maxi-
174 mize the similarity among the resulting complex carriers (see the colored solid
175 lines in Figs.A.1E and A.2E).

176 Taking together, these features are of particular importance to support the
177 link between the spectral group delay consistency (SGDC) defining the time
178 alignment of the modulating components (complex envelopes) with the con-
179 structive interference of the modulated components (complex carriers), which
180 in turn lead to the occurrence of salient events. As a conclusion, the results de-
181 scribed above in connection with the eqs. A.7, A.13, show that the emergence
182 of above-threshold fluctuations in the signal $x(t)$ is related to the consistency
183 of the group delay $\tau(k)$ across the discrete frequency values k . That is, the
184 occurrence of salient events is supported by a slowly varying group delay as a
185 function of the frequency, and this hold true for harmonic, non-harmonic and
186 also for non-uniformly spaced Fourier oscillatory constituents of the signal under
187 analysis.

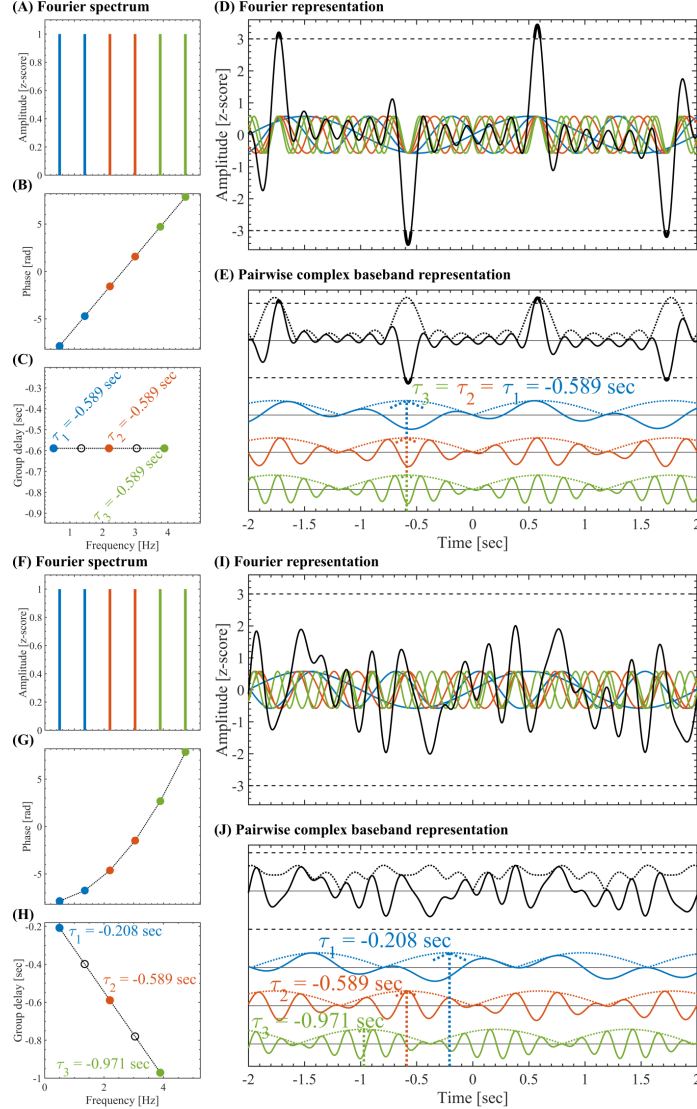


Figure A.1: Pairwise complex baseband representation for a set of oscillatory components with $A_k = \text{cte}$. (A) Set of constant-amplitude $A(k) = 1$ oscillatory components uniformly spaced ($f_s \Delta\omega/(2\pi) = 1.2/\sqrt{2}$ Hz) and having non-harmonic frequencies $f_s \omega(k)/(2\pi) = 0.5 + k f_s \Delta\omega/(2\pi) \in [0.5 - 5]$ Hz, where $f_s = 1024$ Hz is the sampling rate. The pairwise complex baseband representation (eq. A.13) was obtained by grouping the oscillatory components in adjacent non-overlapping pairs color-coded in blue, red and green. (B) Phases $\phi(k)$ having a linear dependence as a function of the frequency within the range $\phi(k) \in 2.5 [-\pi, \pi]$. (C) Group delay $\tau(k)/f_s = -\Delta\phi(k)/(f_s \Delta\omega)$ for the pairs of adjacent oscillatory components. The color-coded filled markers correspond to the $\tau(2k)/f_s$ values, and the black empty markers correspond to $\tau(2k+1)/f_s$ values (see eq. A.13). (D) Z-scored signals. The solid color-coded lines represent the individual oscillatory components, the solid black line is the resulting signal $x(t)$, the horizontal dashed black lines indicate the threshold at $|z| = 3$. (E) Pairwise complex baseband representation. The solid color-coded lines represent the individual amplitude modulated signals (pairs of adjacent oscillatory components), the solid black line is the resulting signal $x(t)$, the color-coded and black dotted lines are the corresponding amplitude envelopes. (F - J) Same as panels (A - E), this time with phases $\phi(k)$ having a quadratic dependence as a function of the frequency within the range $\phi(k) \in 2.5 [-\pi, \pi]$ (see panel G).

188 The group delay is defined in terms of the rate of change of the phase with
189 the frequency, being independent on the amplitude of the spectral components.
190 As a consequence, the consistency of the spectral group delay as a mechanism
191 supporting the emergence of salient events is also valid for spectral profiles other
192 than the constant-amplitude spectrum shown in the Fig. A.1. The Fig. A.2
193 shows the results for a spectral profile given by a set of (uniformly spaced) non-
194 harmonic oscillatory components with amplitudes $A(k) \propto 1/\sqrt{k}$, that is, the
195 power of the spectral components $A^2(k)$ is proportional to $1/k$ (see Figs. A.2A
196 and A.2F). Figs. A.2A-E show the case in which the phases $\phi(k)$ of the spec-
197 tral components $A(k) e^{i(\omega(k)t+\phi(k))}$ in eq. A.12 are randomly distributed in a
198 very small range around zero ($\phi(k) \in [-\pi/10, \pi/10]$). Under this condition, the
199 pairwise complex baseband representation (eq. A.13) shown in the Fig. A.2E is
200 constituted by amplitude modulated signals highly aligned in time. As a con-
201 sequence, prominent salient events can be distinguished in the resulting signal
202 (see solid black line in panels D and E of Fig. A.2). On the other hand, Figs.
203 A.2A-E show the case in which the phase values $\phi(k)$ are randomly distributed
204 in a wider range $\phi(k) \in [-\pi, \pi]$. Under this condition, the pairwise complex
205 baseband representation (eq. A.13) shown in the Fig. A.2J is constituted by
206 amplitude modulated signals non-aligned in time. As a consequence, the result-
207 ing signal $x(t)$ only discloses sub-threshold excursions of amplitude (see solid
208 black line in panels I and J of Fig. A.2).

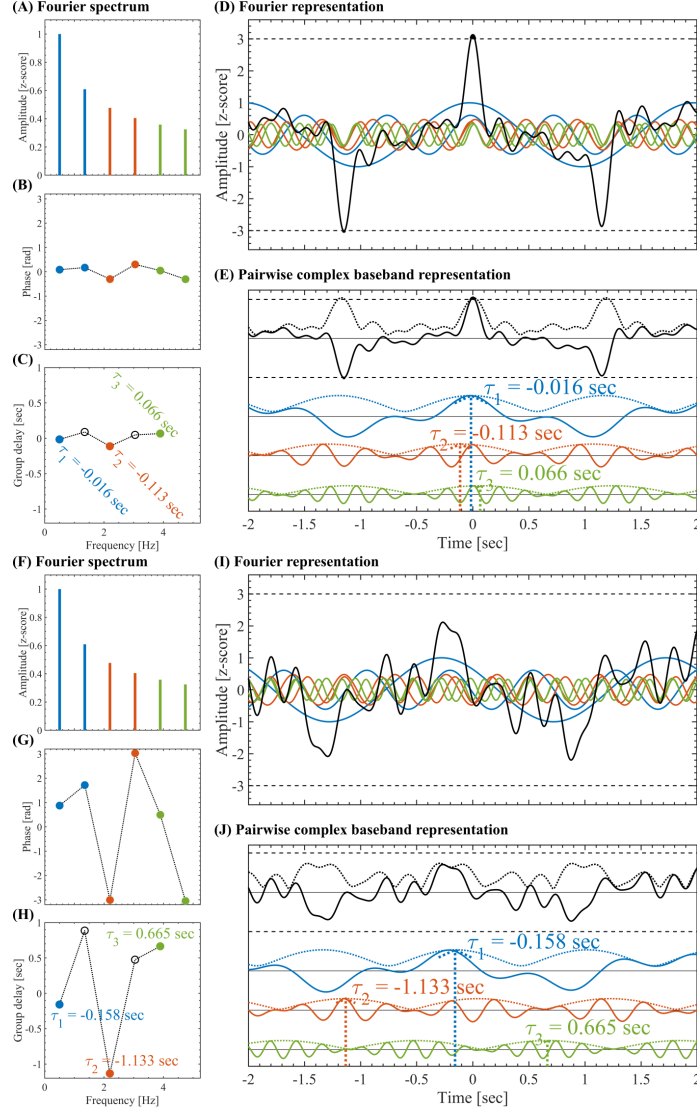


Figure A.2: Pairwise complex baseband representation for a set of oscillatory components with $A(k) \propto 1/\sqrt{k}$. (A) Set of non-constant amplitude $A(k) \propto 1/\sqrt{k}$ oscillatory components uniformly spaced ($f_s \Delta\omega/(2\pi) = 1.2/\sqrt{2}$ Hz) and having non-harmonic frequencies $f_s \omega(k)/(2\pi) = 0.5 + k f_s \Delta\omega/(2\pi) \in [0.5 - 5]$ Hz, where $f_s = 1024$ Hz is the sampling rate. The pairwise complex baseband representation (eq. A.13) was obtained by grouping the oscillatory components in adjacent non-overlapping pairs color-coded in blue, red and green. (B) Phases $\phi(k)$ randomly distributed within a very small range around zero ($\phi(k) \in [-\pi/10, \pi/10]$). (C) Group delay $\tau(k)/f_s = -\Delta\phi(k)/(f_s \Delta\omega)$ for the pairs of adjacent oscillatory components. The color-coded filled markers correspond to the $\tau(2k)/f_s$ values, and the black empty markers correspond to $\tau(2k+1)/f_s$ values (see eq. A.13). (D) Z-scored signals. The solid color-coded lines represent the individual oscillatory components, the solid black line is the resulting signal $x(t)$, the horizontal dashed black lines indicate the threshold at $|z| = 3$. (E) Pairwise complex baseband representation. The solid color-coded lines represent the individual amplitude modulated signals (pairs of adjacent oscillatory components), the solid black line is the resulting signal $x(t)$, the color-coded and black dotted lines are the corresponding amplitude envelopes. (F - J) Same as panels (A - E), this time the phases $\phi(k)$ are randomly distributed within the range $\phi(k) \in [-\pi, \pi]$ (see panel G).

209 In summary, the analytical arguments presented above, condensed in the eqs.
 210 A.7 - A.10 and A.13 - A.16, allowed us to identify the consistency of the group
 211 delay across the spectral components as a mechanism explaining the emergence
 212 of above-threshold fluctuations from the Fourier oscillatory constituents of the
 213 activity associated with a single brain region. In the next section we describe
 214 the signal processing tools proposed to quantify the SGDC in empirical data.

215 *Appendix A.3. Measures to assess the spectral group delay consistency*

216 The analytical arguments presented in the Appendix A.2 have profound con-
 217 sequences regarding the interpretation of the experimental results in connection
 218 with the emergence of salient events from narrowband oscillations and broad-
 219 band $1/f$ activity. Specifically, the pairwise complex baseband representation
 220 of band-limited signals (eqs. A.7 - A.10 and A.13 - A.16), explicitly shows that
 221 the mechanism underlying the emergence of above-threshold fluctuations in a
 222 signal $x(t)$ can be understood in terms of the consistency of the group delay
 223 across the Fourier oscillatory constituents of the signal (see the complex en-
 224 velopes $\tilde{x}_k(t - \tau(k))$ in eqs. A.10 and A.16). By considering a multi-regional
 225 approach, the pairwise complex baseband representation can be applied on the
 226 activity $x_r(t)$ of each brain region r , to obtain complex envelopes of the form
 227 $\tilde{x}_{r,k}(t - \tau_r(k))$. Here we recall that $\tilde{x}_{r,k}(t - \tau_r(k))$ determine the envelopes of
 228 the individual amplitude modulated signals constituting the signal $x_r(t)$ (see
 229 the solid and doted color-coded curves in the Figs. A.1E,J and A.2E,J). Hence,
 230 the consistency of the spectral group delay $\tau_r(k)$ determines the synchronization
 231 of the complex envelopes $\tilde{x}_{r,k}(t - \tau_r(k))$ across both frequency values $\omega(k)$ and
 232 brain regions r . In what follows we describe the proposed measures designed
 233 to quantify the spectral group delay consistency (SGDC) in experimental data
 234 across either frequency values and/or brain regions. In order to simplify the no-
 235 tation, in the rest of this section we will use ω instead of the discrete frequency
 236 index k , implicitly assuming that $\omega = \omega(k)$. In the most general case, the spec-
 237 tral group delay can be estimated as $\tau_r(\omega) = -\Delta\phi_r(\omega)/\Delta\omega(\omega)$, where $\Delta\phi_r(\omega)$
 238 and $\Delta\omega(\omega)$ are the incremental phase and incremental frequency between adja-
 239 cent spectral components associated with the activity $x_r(t)$ of the brain region
 240 r , respectively. Let us consider first the particular case of $\Delta\omega(\omega) = \Delta\omega = \text{cte.}$,
 241 in which the group delay results $\tau_r(\omega) \propto -\Delta\phi_r(\omega)$. Therefore, the SGDC can
 242 be simply assessed via the Euler's transform of the incremental phase as follows,

$$SGDC(r) = \frac{1}{N} \sum_{\omega} e^{-i\Delta\phi_r(\omega)} : \Delta\omega = \text{cte. across } r \quad (\text{A.18})$$

$$SGDC(\omega) = \frac{1}{N} \sum_r e^{-i\Delta\phi_r(\omega)} : \Delta\omega = \text{cte. across } \omega \quad (\text{A.19})$$

243 The modulus of eqs. A.18 and A.19 satisfies,

$$|SGDC| = \left| \frac{1}{N} \sum e^{-i\Delta\phi_r(\omega)} \right| = R = (1 - S) \in [0, 1] \quad (\text{A.20})$$

In the eqs. A.18, A.19 and A.20, N is the number of either frequency values or brain regions as appropriate, R is the resultant vector length and S is the circular variance [47]. The eq. A.20 explicitly shows that the SGDC is assessed as one minus the circular variance of the incremental phase. The definition of the SGDC measures given in the eqs. A.18, A.19 and A.20 should not be confused with the traditional measure for quantifying coherence known as Phase Locking Value (PLV) [48, 49]. Specifically, the SGDC measures as defined in the eqs. A.18, A.19 and A.20 assess the consistency of the incremental phase $\Delta\phi_r(\omega)$ across the frequency values ω . In contrast, the PLV assesses the consistency of phase difference across the time samples, where the phase difference is computed between two phase time series corresponding to two specific frequency bands in the same or different brain regions [48, 49]. As stated in the eq. A.18, the $SGDC(r)$ is a bounded measure in the range $[0, 1]$ and quantifies how much the group delay varies across the spectral components conforming the activity of interest $x_r(t)$. On the one hand, constant group delay values $\tau_r(\omega) \propto -\Delta\phi_r(\omega)$ across the spectral components produce $|SGDC(r)| \approx 1$ indicating a high SGDC, which is associated with high burstiness of the signal $x_r(t)$ (see Figs. A.1A-E and A.2A-E). On the other hand, in the case of group delay values varying randomly (or non-linearly) across the spectral components produces $|SGDC(r)| \approx 0$ indicating low SGDC associated with low burstiness of the signal $x_r(t)$ (see Figs. A.1F-J and A.2F-J). Similarly, the $SGDC(\omega)$ defined in the eq. A.19 is a bounded measure in the range $[0, 1]$ and quantifies how much the spectral group delay at a given frequency ω , varies across the brain regions r . On the one hand, constant group delay values $\tau_r(\omega) \propto -\Delta\phi_r(\omega)$ across the brain regions produce $|SGDC(\omega)| \approx 1$ indicating a high group delay consistency, which is associated with high cross-regional synchronization of the bursts at a given frequency ω . On the other hand, in the case of group delay values varying randomly (or non-linearly) across the brain regions produces $|SGDC(\omega)| \approx 0$ indicating low group delay consistency associated with low cross-regional synchronization of the bursts at a given frequency ω . Now we will consider the more general case in which $\Delta\omega(k) \neq \text{cte}$. In line with the previous analysis, the SGDC measures can be defined in terms of the linear variance of the group delay $Var(\tau)$ as follows,

$$SGDC = 1 - \frac{Var(\tau)}{\max\{Var(\tau)\}} \in [0, 1] \quad (\text{A.21})$$

$$Var(\tau) = \frac{1}{N} \sum (\tau - \langle \tau \rangle)^2 \quad (\text{A.22})$$

In the eq. A.22, the mean group delay value $\langle \tau \rangle$ and the sum associated with the linear variance $Var(\tau)$ are computed across the N frequency values ω or brain regions r in which case the eq. A.21 produces $SGDC(r)$ or $SGDC(\omega)$, respectively. Importantly, the eqs. A.18, A.19 and A.21 constitute a specialized framework to quantify the emergence of large-scale bursts (i.e., brain avalanches) from the brain activity. That is, the $SGDC(r)$ measure assesses the emergence of local above-threshold fluctuations from the spectral components constituting the activity of a single brain region, whereas the $SGDC(\omega)$ measure quantifies

285 the synchronization of the above-threshold bursts across brain regions. In line
 286 with this, we introduce the pairwise spectral group delay consistency (pSGDC)
 287 to quantify the burstiness and cross-regional bursts synchronization in a single
 288 measure. In the case of $\Delta\omega(\omega) = \Delta\omega = \text{cte.}$, the pSGDC is defined as follows,

$$pSGDC(r_1, r_2) = \frac{\left(\underbrace{SGDC(r_1) + SGDC(r_2)}_{\text{Mean pairwise burstiness}} \right)}{2} \underbrace{\frac{1}{N} \sum_{\omega} e^{-i(\Delta\phi_1(\omega) - \Delta\phi_2(\omega))}}_{\text{Correlation of burstiness across } \omega} \quad (\text{A.23})$$

: $\Delta\omega = \text{cte.}$ across r

289 In the eq. A.23, the quantities $SGDC(r_1)$ and $SGDC(r_2)$ are computed using
 290 the eq. A.18. In the case of $\Delta\omega(\omega) \neq \text{cte}$ the pSGDC is defined as follows,

$$pSGDC(r_1, r_2) = \frac{\left(\underbrace{SGDC(r_1) + SGDC(r_2)}_{\text{Mean pairwise burstiness}} \right)}{2} \underbrace{\frac{\text{Cov}(\tau_1(\omega), \tau_2(\omega))}{\text{Var}(\tau_1(\omega)) \text{Var}(\tau_2(\omega))}}_{\text{Correlation of burstiness across } \omega} \quad (\text{A.24})$$

$\text{Cov}(\tau_1(\omega), \tau_2(\omega)) = \frac{1}{N} \sum_{\omega} (\tau_1(\omega) - \langle \tau_1(\omega) \rangle)(\tau_2(\omega) - \langle \tau_2(\omega) \rangle)$

291 In the eq. A.24, the quantities $SGDC(r_1)$ and $SGDC(r_2)$ are computed using
 292 the eqs. A.21 and A.22. Besides, the quantities $\text{Var}(\tau_1(\omega))$ and $\text{Var}(\tau_2(\omega))$ are
 293 computed using the eq. A.22. In both cases the sum associated with the eq.
 294 A.22 is computed over the frequency values ω . The eqs. A.23 and A.24 show that
 295 the $pSGDC(r_1, r_2)$ is a linear measure conformed by a factor quantifying the
 296 cross-regional correlation between the group delays across the frequency values,
 297 weighted by a coefficient quantifying the burstiness of the two involved brain
 298 regions (r_1, r_2) . Importantly, we found that the pSGDC performs similarly to
 299 the cokurtosis (fourth standardized cross central moment) [43] in reproducing
 300 the observed avalanche topographies and co-activation patterns (see Fig. 6 in
 301 Section 3.6 of the main text). This is particularly interesting taking into ac-
 302 count that these two non-time-resolved measures (i.e., computed on the whole
 303 time series) effectively reproduce the avalanche topographies through two dif-
 304 ferent approaches. That is, the cokurtosis is a non-linear time-domain measure,
 305 whereas the pSGDC is a linear measure entirely based on the frequency-domain.
 306 Moreover, the pSGDC and cokurtosis disclose a better performance to reproduce
 307 the observed avalanche topographies and co-activation patterns when compared
 308 to the kurtosis (scaled version of the fourth central moment) and the Pearson's
 309 linear correlation (see discussion in Section 3.6 of the main text). These results
 310 are consistent with the fact that kurtosis measures the presence of outliers (tails
 311 of the distribution of amplitude values) and the Pearson's correlation coefficient
 312 the linear correlations between the two time series. On the other hand, pSGDC
 313 and cokurtosis measures quantify these two features simultaneously. In this
 314 work the kurtosis (K) and the cokurtosis (CK) were assessed via the following

³¹⁵ expressions,

$$\begin{aligned} K(r) &= \frac{(N_s - 1)}{(N_s - 2)(N_s - 3)} ((N_s + 1)k(r) - 3(N_s - 1)) \quad (\text{A.25}) \\ k(r) &= \frac{\mu_{r,4}}{\sigma_r^4} \\ \mu_{r,4} &= \frac{1}{N_s} \sum_t (x_r - \langle x_r \rangle)^4 \\ \sigma_r^4 &= \left(\frac{1}{N_s} \sum_t (x_r - \langle x_r \rangle)^2 \right)^2 \end{aligned}$$

³¹⁶

$$\begin{aligned} CK(r_1, r_2) &= \frac{ck(r_1, r_2)}{\sigma_1^2 \sigma_2^2} \quad (\text{A.26}) \\ ck(r_1, r_2) &= \frac{1}{N_s} \sum_t (x_1 - \langle x_1 \rangle)^2 (x_2 - \langle x_2 \rangle)^2 \\ \sigma_r^2 &= \frac{1}{N_s} \sum_t (x_r - \langle x_r \rangle)^2 \end{aligned}$$

³¹⁷ In the eqs. A.25 and A.26, N_s is the number of time samples and $\langle \cdot \rangle$ stands for
³¹⁸ mean value across the time samples.

³¹⁹ In the rest of this section, we present illustrative examples using the eqs. A.18
³²⁰ and A.19 on synthetic multi-channel bursts emerging from narrowband oscillatory
³²¹ activity. Fig. A.3 shows the $|SGDC(r)|$ computed using the eq. A.18 for
³²² three time series synthesized using the Eq. A.11. In each channel, the signal
³²³ was synthesized by the linear superposition of 10 sinusoidal tones with uniformly
³²⁴ spaced frequencies ($\Delta\omega = \text{cte.}$) in the range $f_s \omega/(2\pi) \in [0.5 - 3]$ Hz. In channels
³²⁵ 1 and 2, the phase of the tones were set as a quadratic function of the frequency
³²⁶ within the range $\phi_1(\omega) \propto 2\pi\omega^2 \in [-2\pi, 2\pi]$ and $\phi_2(\omega) \propto \pi\omega^2 \in [-\pi, \pi]$, re-
³²⁷ spectively. In channel 3, the phase of the tones were set as a linear function of
³²⁸ the frequency within the range $\phi_3(\omega) \propto \pi\omega \in [-\pi, \pi]$. Fig. A.3B shows that
³²⁹ the higher the burstiness (i.e., amplitude of the transient fluctuations) disclosed
³³⁰ by the resulting signal (see solid black line in the Fig. A.3A), the higher the
³³¹ $|SGDC(r)|$ value. The channel 3, corresponding to the tones having a linear
³³² phase dependence with the frequency, discloses the maximum $|SGDC(r)| \approx 1$.

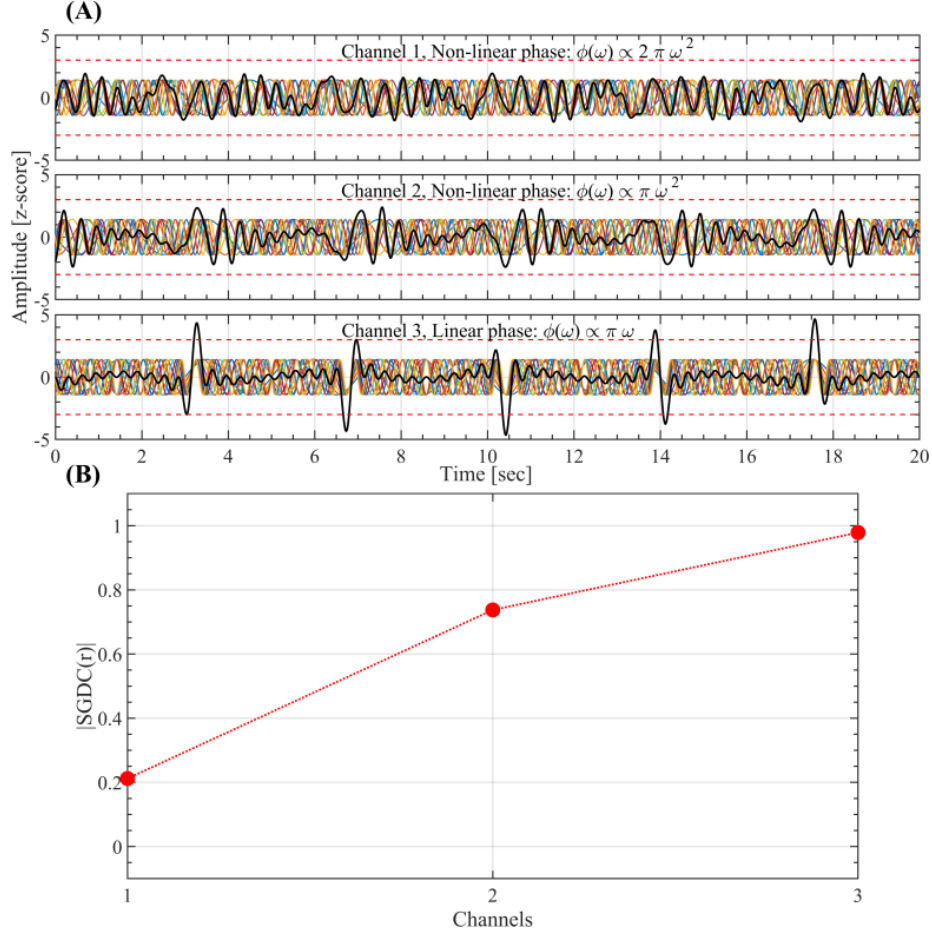


Figure A.3: $SGDC(r)$ computed using the eq. A.18 on a multi-channel configuration. (A) Three time series $x_r(t)$ (black solid lines) synthesized using the Eq. A.11. In each channel, the signal $x_r(t)$ was synthesized by the linear superposition of 10 sinusoidal tones (colored solid lines) with unitary amplitude and uniformly spaced frequencies ($f_s \Delta\omega/(2\pi) = 0.278$ Hz) within the range $f_s \omega(k)/(2\pi) = 0.5 + k f_s \Delta\omega/(2\pi) \in [0.5 - 3]$ Hz. In the channels 1 and 2, the phase of the tones were set as a quadratic function of the frequency within the range $\phi_1(\omega) \propto 2\pi\omega^2 \in [-2\pi, 2\pi]$ and $\phi_2(\omega) \propto \pi\omega^2 \in [-\pi, \pi]$, respectively. In the channel 3, the phase of the tones were set as a linear function of the frequency within the range $\phi_3(\omega) \propto \pi\omega \in [-\pi, \pi]$. (B) Modulus of the $SGDC(r)$ for each channel. Note that the higher the burstiness (i.e., amplitude of the transient fluctuations) disclosed by the resulting signal (see solid black line in the panel A), the higher the $|SGDC(r)|$ value. As expected, the channel 3 corresponding to the tones having a linear phase dependence with the frequency discloses the maximum $|SGDC(r)| \approx 1$.

³³³ Figs. A.4 and A.5 show the $SGDC(\omega)$ computed using the eq. A.19 com-
³³⁴ pared against the Phase Locking Value (PLV) assessed using the following ex-

³³⁵ pression [48, 49],

$$PLV = \frac{1}{N} \sum_t e^{i(n\psi(t) - m\theta(t))} \quad (\text{A.27})$$

³³⁶ In eq. A.27, $\psi(t)$ and $\theta(t)$ are the phase time series of interest and the integers
³³⁷ $n, m \in \mathbb{N}$ are required to allow the comparison of phase time series pertaining to
³³⁸ different frequency bands. Of note, the $SGDC(\omega)$ quantifies, at each frequency
³³⁹ value, the bursts synchronization across the brain regions (channels), whereas
³⁴⁰ the PLV quantifies either local or cross-regional phase coherence between two
³⁴¹ frequency bands and it is not related to the signal burstiness, i.e., the PLV
³⁴² is not sensitive to the emergence of above-threshold fluctuations neither to the
³⁴³ cross-regional synchronization of salient events. Fig. A.4A shows three channels
³⁴⁴ in which the resulting time series (solid black line) have been synthesized as the
³⁴⁵ linear superposition of 10 sinusoidal tones with uniformly spaced frequencies
³⁴⁶ ($\Delta\omega = \text{cte.}$) in the range $f_s \omega/(2\pi) \in [0.5 - 3]$ Hz (see Eq. A.11). In each
³⁴⁷ channel, the phase of all the oscillatory components was set to zero ($\phi_r(\omega) = 0 \forall \omega$). The local and cross-regional effects of this setup can be summarized as
³⁴⁸ follows,

- ³⁵⁰ • In each channel (local effect), we obtain the maximum group delay consistency
³⁵¹ across frequency values explaining the emergence of above-threshold
³⁵² fluctuations. That is, $\phi_r(\omega) = 0 \implies \Delta\phi_r(\omega) = 0 \implies \tau_r(\omega) = -\Delta\phi_r/\Delta\omega = 0 = \text{cte} \implies SGDC(r) = 1 : r = 1, 2, 3$ (data not shown).
- ³⁵⁴ • At each frequency, we obtain the maximum group delay consistency across
³⁵⁵ channels (cross-regional effect) explaining the synchronization of the salient
³⁵⁶ events across the channels. That is, $\phi_r(\omega) = 0 \implies \Delta\phi_r(\omega) = 0 \implies \tau_r(\omega) = -\Delta\phi_r/\Delta\omega = 0 = \text{cte} \implies SGDC(\omega) = 1 \forall \omega$. The resulting
³⁵⁷ $|SGDC(\omega)|$ is shown in Fig. A.4B.
- ³⁵⁹ • At each frequency, we obtain the maximum phase coherence across channels
³⁶⁰ (cross-regional effect). That is, $\psi_{r,\omega}(t) - \theta_{r',\omega}(t) = 0 \implies |PLV| = 1 \forall \omega$, where the phase time series $\psi_{r,\omega}(t)$ and $\theta_{r',\omega}(t)$ were extracted from
³⁶¹ different channels ($(r, r') \in \{1, 2, 3\} : r \neq r'$) and evaluated at the same
³⁶² frequency ω . In other words, $\psi_{r,\omega}(t)$ and $\theta_{r',\omega}(t)$ are the phase time se-
³⁶³ ries associated with two tones homologous in frequency and pertaining to
³⁶⁴ different channels. The resulting $|PLV|$ is shown in the Fig. A.4B.

³⁶⁶ Fig. A.4C shows three time series constituted by the same 10 tones used in
³⁶⁷ Fig. A.4A, with the difference that in this case the phase of the tones were
³⁶⁸ set as $\phi_1(\omega) = 0$, $\phi_2(\omega) \propto -3\pi\omega$ and $\phi_3(\omega) \propto +3\pi\omega$ for the channel 1, 2
³⁶⁹ and 3, respectively. The linear phase dependence with the frequency associated
³⁷⁰ with the channels 2 and 3 produces a time-shift in the resulting signals. As a
³⁷¹ consequence, in this multi-channel configuration the resulting above-threshold
³⁷² fluctuations are not synchronized across channels (see the solid black lines in
³⁷³ the Fig. A.4C). In this case, the SGDC and PLV measures result,

- ³⁷⁴ • In each channel (local effect), we obtain the maximum group delay consistency
³⁷⁵ across frequency values explaining the emergence of above-threshold

376 fluctuations. That is, $\Delta\phi_r(\omega) = \text{cte.} \implies \tau_r(\omega) = -\Delta\phi_r/\Delta\omega = \text{cte} \implies$
377 $SGDC(r) = 1 : r = 1, 2, 3$. Note that this result is similar to what we
378 obtained for a constant group delay (i.e., not a function of the frequency)
379 associated with the channel 3 shown in Fig. A.3.

- 380 • At each frequency, we obtain a low group delay consistency across channels
381 (cross-regional effect) explaining the lack synchronization of the salient
382 events across the channels. That is, $\Delta\phi_1(\omega) = 0, \Delta\phi_2(\omega) < 0, \Delta\phi_3(\omega) >$
383 $0 \implies \tau_1(\omega) = 0, \tau_2(\omega) > 0, \tau_3(\omega) < 0 \implies SGDC(\omega) \approx 0 \forall \omega$. The
384 resulting $|SGDC(\omega)|$ is shown in the Fig. A.4D.
- 385 • At each frequency, we obtain the maximum phase coherence across chan-
386 nels (cross-regional effect). That is, $\psi_{r,\omega}(t) - \theta_{r',\omega}(t) = \text{cte.} \implies |PLV| =$
387 $1 \forall \omega$, where the phase time series $\psi_{r,\omega}(t)$ and $\theta_{r',\omega}(t)$ were extracted from
388 different channels ($(r, r') \in \{1, 2, 3\} : r \neq r'$) and evaluated at the same
389 frequency ω . In other words, $\psi_{r,\omega}(t)$ and $\theta_{r',\omega}(t)$ are the phase time se-
390 ries associated with two tones homologous in frequency and pertaining to
391 different channels. The resulting $|PLV|$ is shown in the Fig. A.4D.
- 392 It is essential to note that, the $SGDC(\omega)$ measure is highly sensitive to the
393 cross-regional synchronization of the salient events, whereas the PLV measure
394 is completely blind to this effect (compare Figs. A.4B and A.4D).

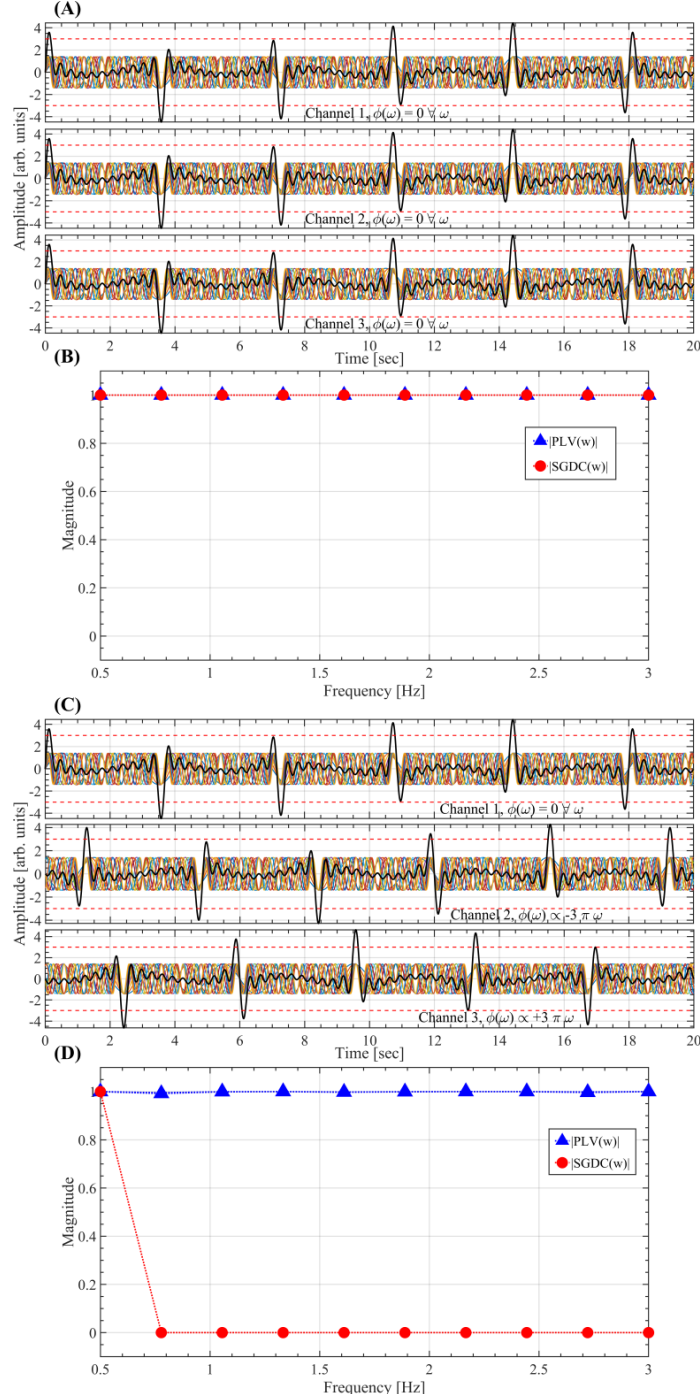


Figure A.4: $SGDC(\omega)$ computed using the eq. A.19 on a multi-channel configuration. (A) Three time series $x_r(t)$ (black solid lines) synthesized using the Eq. A.11. In each channel, the signal $x_r(t)$ was synthesized by the linear superposition of 10 sinusoidal tones (colored solid lines) with unitary amplitude and uniformly spaced frequencies ($f_s \Delta\omega/(2\pi) = 0.278$ Hz) within the range $f_s \omega(k)/(2\pi) = 0.5 + k 18 \Delta\omega/(2\pi) \in [0.5 – 3]$ Hz. In each channel, the phase of all the oscillatory components was set to zero ($\phi_r(\omega) = 0 \forall \omega$). (B) $SGDC(\omega)$ and PLV measures computed using the eqs. A.19 and A.27, respectively, for the multi-channel configuration shown in panel A. (C) Same as in A, but in this case the phase of the tones were set as $\phi_1(\omega) = 0$, $\phi_2(\omega) \propto -3\pi\omega$ and $\phi_3(\omega) \propto +3\pi\omega$ for the channel 1, 2 and 3, respectively. (D) Same as in B for the multi-channel configuration shown in panel C.

³⁹⁵ Fig. A.5A shows three time series constituted by the same 10 tones used in
³⁹⁶ Figs. A.4A and A.4C with the difference that in this case the phase of the tones
³⁹⁷ were set as follows,

$$\begin{aligned}\phi_1(\omega) &= 0 \quad \forall \omega \text{ (LF+HF)} \\ \phi_2(\omega) &\propto \begin{cases} 0, & \forall 0.5\text{Hz} \leq f_s \omega/(2\pi) \leq 1.5\text{Hz} \text{ (LF)} \\ -3\pi\omega, & \forall 1.5\text{Hz} \leq f_s \omega/(2\pi) \leq 3\text{Hz} \text{ (HF)} \end{cases} \\ \phi_3(\omega) &\propto \begin{cases} 0, & \forall 0.5\text{Hz} \leq f_s \omega/(2\pi) \leq 1.5\text{Hz} \text{ (LF)} \\ +3\pi\omega, & \forall 0.5\text{Hz} \leq f_s \omega/(2\pi) \leq 1.5\text{Hz} \text{ (HF)} \end{cases}\end{aligned}\quad (\text{A.28})$$

³⁹⁸ This phase configuration produce LF transient fluctuations co-occurring across
³⁹⁹ the channels, while the resulting HF transient fluctuations are not synchronized
⁴⁰⁰ across the channels (see Fig. A.5A). Importantly, the $SGDC(\omega)$ effectively dis-
⁴⁰¹ criminate the cross-regional synchronization of the transient fluctuations across
⁴⁰² the frequency values, whereas the PLV measure is again completely blind to
⁴⁰³ this effect (see Fig. A.5B). Fig. A.5C shows three time series constituted by
⁴⁰⁴ the same 10 tones used in Fig. A.5A (see Eq. A.11) with the difference that in
⁴⁰⁵ this case the phase of the tones were set as follows,

$$\begin{aligned}\phi_1(\omega) &= 0 \quad \forall \omega \text{ (LF+HF)} \\ \phi_2(\omega) &\propto \begin{cases} -3\pi\omega, & \forall 0.5\text{Hz} \leq f_s \omega/(2\pi) \leq 1.5\text{Hz} \text{ (LF)} \\ 0, & \forall 1.5\text{Hz} \leq f_s \omega/(2\pi) \leq 3\text{Hz} \text{ (HF)} \end{cases} \\ \phi_3(\omega) &\propto \begin{cases} +3\pi\omega, & \forall 0.5\text{Hz} \leq f_s \omega/(2\pi) \leq 1.5\text{Hz} \text{ (LF)} \\ 0, & \forall 0.5\text{Hz} \leq f_s \omega/(2\pi) \leq 1.5\text{Hz} \text{ (HF)} \end{cases}\end{aligned}\quad (\text{A.29})$$

⁴⁰⁶ Similarly to the previous case, the $SGDC(\omega)$ effectively discriminate the cross-
⁴⁰⁷ regional synchronization of the transient fluctuations across the frequency val-
⁴⁰⁸ ues, whereas the PLV measure is again completely blind to this effect (see Fig.
⁴⁰⁹ A.5D). It is worth mentioning that $\Delta\phi_r(\omega)$ in the eq. A.19 is the incremen-
⁴¹⁰ tal phase between adjacent spectral components associated with the activity
⁴¹¹ $x_r(t)$ of the brain region r . Thus, for N spectral components we obtain $N - 1$
⁴¹² incremental phase values $\Delta\phi_r(\omega)$. As a convention, we add an extra value
⁴¹³ $\Delta\phi_r(\omega) = 0$ as the first element (i.e., lowest frequency) of the list of incremental
⁴¹⁴ phase values. Hence, for N spectral components the eqs. A.18 and A.19 pro-
⁴¹⁵ duce N values of SGDC. In particular, the first value (i.e., lowest frequency) of
⁴¹⁶ $SGDC(\omega)$, associated with the artificially added $\Delta\phi_r(\omega) = 0$, is always equal
⁴¹⁷ to 1 (this becomes evident in the Figs. A.4D and A.5D).

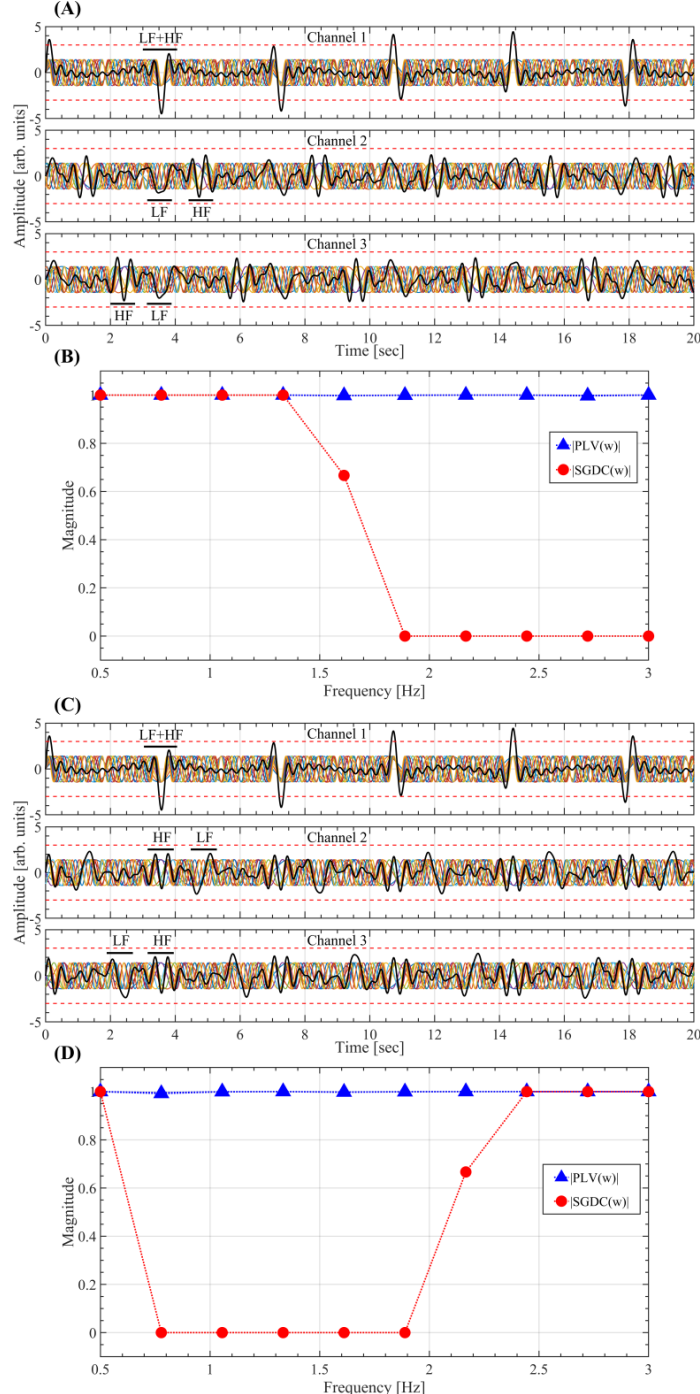


Figure A.5: $SGDC(\omega)$ computed using the eq. A.19 on a multi-channel configuration. (A) Three time series $x_r(t)$ (black solid lines) synthesized using the Eq. A.11. In each channel, the signal $x_r(t)$ was synthesized by the linear superposition of 10 sinusoidal tones (colored solid lines) with unitary amplitude and uniformly spaced frequencies ($f_s \Delta\omega/(2\pi) = 0.278$ Hz) within the range $f_s \omega(k)/(2\pi) = 0.5 + k 20 \Delta\omega/(2\pi) \in [0.5 – 3]$ Hz. In each channel, the phases of the oscillatory components were configured as stated in the set of eqs. A.28. (B) $SGDC(\omega)$ and PLV measures computed using the eqs. A.19 and A.27, respectively, for the multi-channel configuration shown in panel A. (C) Same as in A, but in this case the phase of the tones were configured as stated in the set of eqs. A.29. (D) Same as in B for the multi-channel configuration shown in panel C.

418 *Appendix A.4. Spectral group delay consistency in the surrogate data*

419 Here we analytically show that, on the one hand, A-surrogates significantly
 420 reduce the spectral group delay consistency (SGDC) across both frequency val-
 421 ues ($SGDC(r)$) and brain regions ($SGDC(\omega)$). On the other hand, B-surrogates
 422 significantly reduce the SGDC across frequency values ($SGDC(r)$), while pre-
 423 serving the SGDC across brain regions ($SGDC(\omega)$).

424 We start by recalling the definition of $SGDC(r)$ and $SGDC(\omega)$ for a multi-
 425 regional time series $x_r(t)$,

$$\begin{aligned} \mathfrak{F}\{x_r(t)\} &= X_r(\omega) = A_r(\omega)e^{i\phi_r(\omega)} \\ \Delta\phi_r(\omega) &= \phi_r(\omega + \Delta\omega) - \phi_r(\omega) \\ SGDC(r) &= \frac{1}{N} \sum_{\omega} e^{-i\Delta\phi_r(\omega)} : \Delta\omega = \text{cte. across } r \end{aligned} \quad (\text{A.30})$$

$$SGDC(\omega) = \frac{1}{N} \sum_r e^{-i\Delta\phi_r(\omega)} : \Delta\omega = \text{cte. across } \omega \quad (\text{A.31})$$

426 where $A_r(\omega)$ and $\phi_r(\omega)$ are the amplitude and phase Fourier spectra, respec-
 427 tively. In eqs. A.30 and A.31, N is the number of either frequency values
 428 or brain regions, respectively, and $\Delta\phi_r(\omega)$ is the incremental phase computed
 429 across the spectral components of the DFT spectrum $X_r(\omega)$ associated with
 430 the signals $x_r(t)$. In the case of the surrogate multi-regional time series $x_r^s(t)$,
 431 obtained by phase randomization of the original time series in the frequency
 432 domain, we have,

$$\begin{aligned} \mathfrak{F}\{x_r^s(t)\} &= X_r^s(\omega) = A_r(\omega)e^{i(\phi_r(\omega)+\theta_r(\omega))} \\ SGDC^s(r) &= \frac{1}{N} \sum_{\omega} e^{-i(\Delta\phi_r(\omega)+\Delta\theta_r(\omega))} : \Delta\omega = \text{cte. across } r \end{aligned} \quad (\text{A.32})$$

$$SGDC^s(\omega) = \frac{1}{N} \sum_r e^{-i(\Delta\phi_r(\omega)+\Delta\theta_r(\omega))} : \Delta\omega = \text{cte. across } \omega \quad (\text{A.33})$$

433 In the eqs. A.32 and A.33, $\Delta\theta_r(\omega)$ is the incremental phase associated with the
 434 random phase-shift $\theta_r(\omega)$ extracted from the surrogate DFT spectrum $X_r^s(\omega)$
 435 of each brain region r . Let us consider two extreme cases derived from the eqs.
 436 A.30 and A.32 with $\Delta\theta_r(\omega)$ varying randomly across ω ,

- 437 1 For $\Delta\phi_r(\omega) \approx \text{cte.} \implies |SGDC(r)| \approx 1 > |SGDC^s(r)| \approx 0$.
 438 2 For $\Delta\phi_r(\omega)$ varying randomly across $\omega \implies |SGDC(r)| \approx |SGDC^s(r)| \approx 0$.

439 From these two extreme cases we infer that, for $\theta_r(\omega)$ varying randomly across
 440 ω , $|SGDC(r)|$ is the upper bound of $|SGDC^s(r)|$. As a consequence, for the A-
 441 and B-surrogates in general we obtain $|SGDC^s(r)| < |SGDC(r)|$. Similarly, in
 442 the case of A-surrogates computed with $\theta_r(\omega)$ varying randomly across the brain
 443 regions r , eqs. A.31 and A.33 in general produce $|SGDC^s(\omega)| < |SGDC(\omega)|$.
 444 In the particular case of the B-surrogates, at each frequency ω we add the
 445 same phase-shift value $\theta_r(\omega)$ in all the brain regions r , producing $\Delta\theta_r(\omega) =$

⁴⁴⁶ $\Delta\theta(\omega)$ $\forall 1 \leq r \leq N$. As a consequence, by taking the modulus in both sides
⁴⁴⁷ of the eq. A.33 we obtain the equivalence between the true data and the B-
⁴⁴⁸ surrogate in terms of $|SGDC(\omega)|$,

$$\begin{aligned} |SGDC^s(\omega)| &= \left| e^{-i\Delta\theta(\omega)} \frac{1}{N} \sum_r e^{-i\Delta\phi_r(\omega)} \right| \\ &= |e^{-i\Delta\theta(\omega)} SGDC(\omega)| \\ &= |SGDC(\omega)| \end{aligned}$$

⁴⁴⁹ It is important to note that this equivalence between the true data and the
⁴⁵⁰ B-surrogate in terms of $|SGDC(\omega)|$ holds only when the $SGDC(\omega)$ measure is
⁴⁵¹ computed on the whole time series (i.e., the non-time-resolved case). That is,
⁴⁵² if the $SGDC(\omega)$ measure is computed in a time-resolved manner around each
⁴⁵³ avalanche, the equivalence between the true data and the B-surrogate in terms
⁴⁵⁴ of $|SGDC(\omega)|$ is not longer true (see Fig. B.10F).

455 **Appendix B. Supplementary results**

456 *Appendix B.1. Supplementary modeling results*

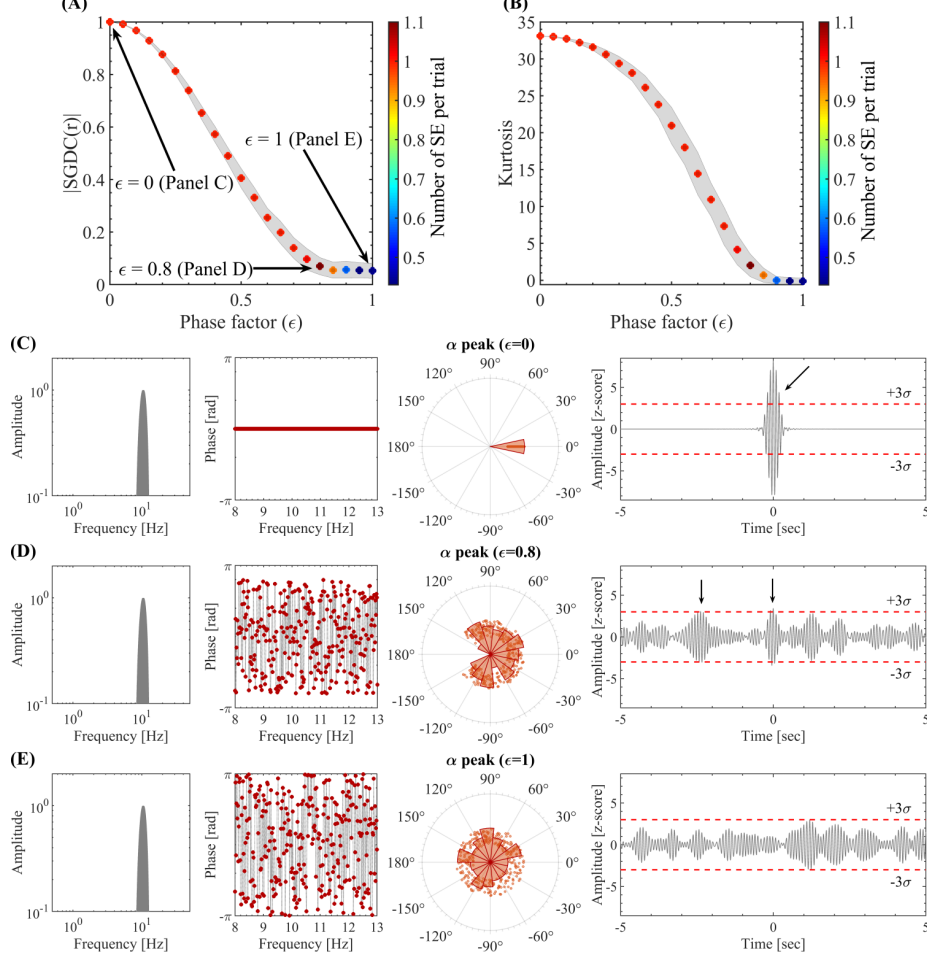


Figure B.6: Spectral group delay consistency underlies the emergence of local above-threshold fluctuations from narrowband oscillations. (A) Spectral group delay consistency, as quantified by the $SGDC(r)$ measure, as a function of the phase factor values. The colored markers indicate the mean $|SGDC(r)|$ value across 100 trials. The shaded error bars in gray correspond to the standard deviation around the mean value. The pseudocolor scale represents the mean number of SE per trial. The $SGDC(r)$ measure was obtained by computing the Equation 1 on the synthetic phase values assigned to the spectral components in the alpha band. (B) Same as in A for the Kurtosis of the amplitude values obtained by computing the Equation A.25 on the signals in time domain. (C) Amplitude spectrum (left), phase spectrum and distribution (middle), and resulting time series (right) corresponding to the signal model for a phase factor $\epsilon = 0$. For the amplitude spectrum we used a Hann window with a null-to-null bandwidth $= 8\text{-}13 \text{ Hz}$, frequency resolution $df = 1/60\text{sec} \approx 0.017 \text{ Hz}$. The phase values of the spectral components were constrained within the range $[-\epsilon\pi, \epsilon\pi]$ and disclosing a random dependence with the frequency. The black arrows in the right-most panel highlight the above-threshold fluctuations disclosed by the signal. (D) Same as in C for a phase factor $\epsilon = 0.8$. (E) Same as in C for a phase factor $\epsilon = 1$. Symbols and abbreviations: SE, Salient Events.

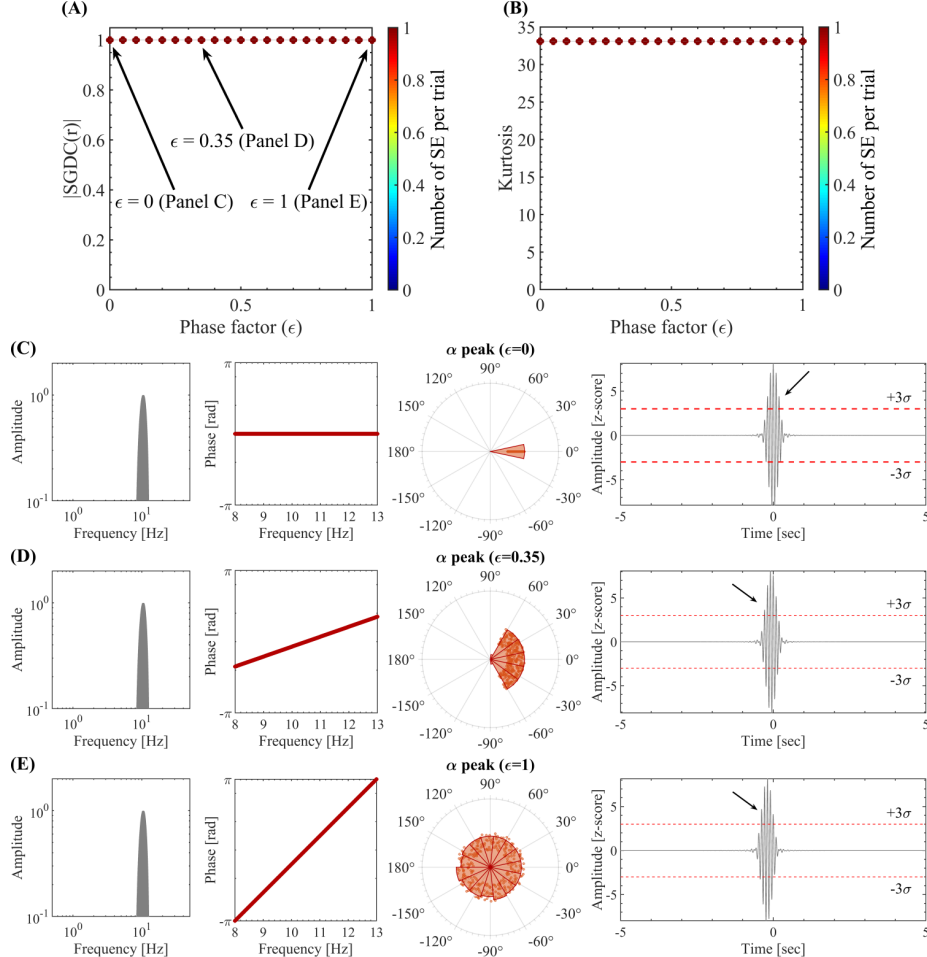


Figure B.7: Spectral group delay consistency underlies the emergence of local above-threshold fluctuations from narrowband oscillations. (A) Spectral group delay consistency, as quantified by the $SGDC(r)$ measure, as a function of the phase factor values. The colored markers indicate the mean $|SGDC(r)|$ value across 100 trials. The shaded error bars in gray correspond to the standard deviation around the mean value. The pseudocolor scale represents the mean number of SE per trial. The $SGDC(r)$ measure was obtained by computing the Equation 1 on the synthetic phase values assigned to the spectral components in the alpha band. (B) Same as in A for the Kurtosis of the amplitude values obtained by computing the Equation A.25 on the signals in time domain. (C) Amplitude spectrum (left), phase spectrum and distribution (middle), and resulting time series (right) corresponding to the signal model for a phase factor $\epsilon = 0$. For the amplitude spectrum we used a Hann window with a null-to-null bandwidth $= 8-13$ Hz, frequency resolution $df = 1/60sec \approx 0.017$ Hz. The phase values of the spectral components were constrained within the range $[-\epsilon\pi, \epsilon\pi]$ and disclosing a linear dependence with the frequency. The black arrows in the right-most panel highlight the above-threshold fluctuations disclosed by the signal. (D) Same as in C for a phase factor $\epsilon = 0.8$. (E) Same as in C for a phase factor $\epsilon = 1$. Symbols and abbreviations: SE, Salient Events.

457 *Appendix B.2. Supplementary results including the deep sources*

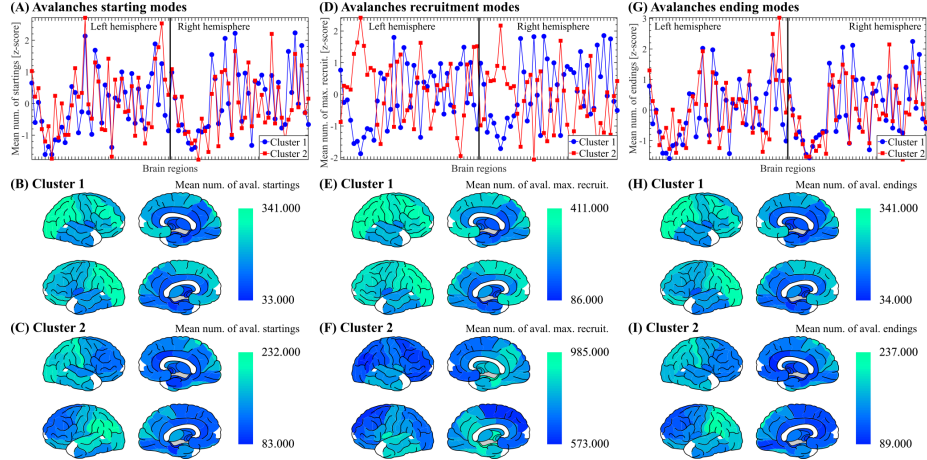


Figure B.8: Avalanches propagation modes. (A) Spatial profile for the avalanches starting modes (see Methods) corresponding to the two avalanche clusters (mean value across 41 participants). The avalanches obtained from 41 subjects were clustered using the Louvain algorithm (resolution parameter $\gamma = 1$, see Methods). The Pearson's correlation between the spatial profiles of cluster 1 and cluster 2 is $r = 0.708$, $P < 0.001$. (B) Brain topographies for the starting modes of cluster 1 avalanches as shown in panel A. (C) Brain topographies for the starting modes of cluster 2 avalanches as shown in panel A. (D-F) Same as A-B for avalanches maximum recruitment modes (see Methods). In panel D, the Pearson's correlation between the spatial profiles of cluster 1 and cluster 2 is $r = -0.841$, $P < 0.001$. (G-I) Same as A-B for avalanches ending modes (see Methods). In panel G, the Pearson's correlation between the spatial profiles of cluster 1 and cluster 2 is $r = 0.718$, $P < 0.001$. The reported P values for the statistical significance of the Pearson's correlation were assessed using Student's t distributions of the two-tailed hypothesis test under the null hypothesis that the correlation is zero.

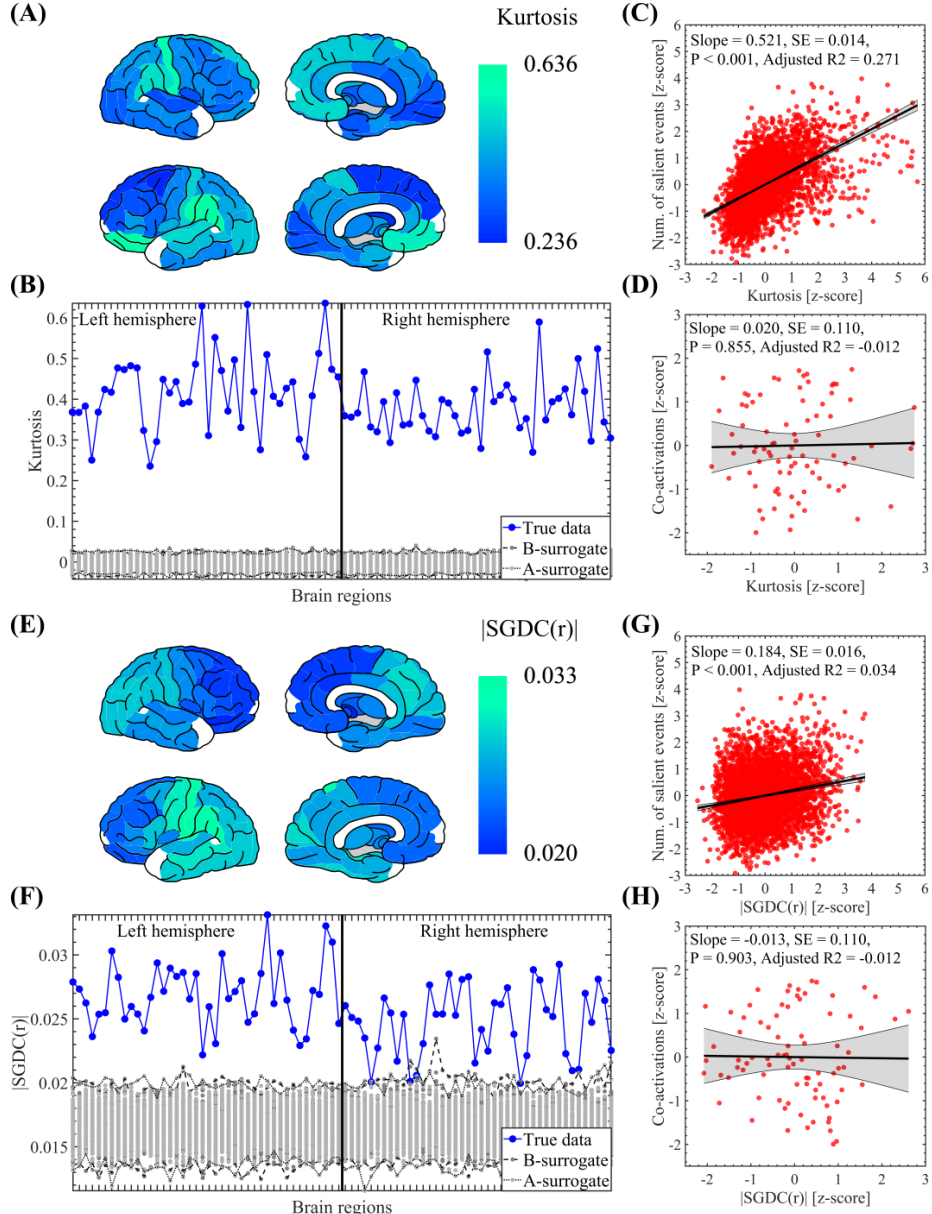


Figure B.9: Measures capturing the local salient events topographies. (A) Brain topographies for the mean kurtosis of each brain region as shown in panel B. (B) Spatial profile showing the mean kurtosis computed on the whole time series (1 min in length) of each brain region (mean value across the 47 participants, see Methods). (C) Scatter plot showing the correlation between the number of salient events and kurtosis spatial profile. Number of samples (red circles) = Number of brain regions × Number of patients = 84 × 47 = 3948. The thick black line and black shaded error bars represent the linear regression and the 95% confidence interval, respectively. (D) Scatter plot showing the correlation between the co-activation (Figure 6B) and kurtosis (panel B) spatial profiles. Number of samples (red circles) = 84. The thick black line and black shaded error bars represent the linear regression and the 95% confidence interval, respectively. (E-H) Same as in A-D for the $SGDC(r)$ measure. In panels C, D, G and H, the reported P values for the statistical significance of the linear regression were assessed using Student's t distributions of the two-tailed hypothesis test under the null hypothesis that the correlation is zero.

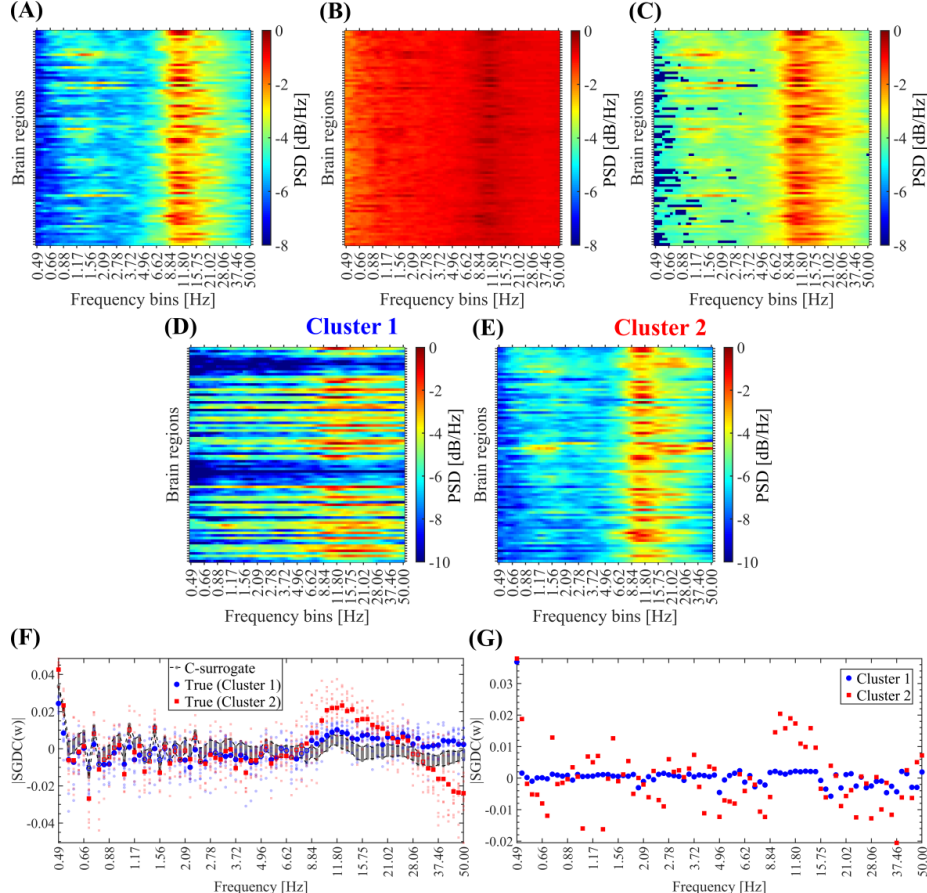


Figure B.10: Transient cross-regional coherence around the alpha band is mainly associated with neuronal avalanches. (A) Mean ASM resulting from the average across the true avalanches detected in 10 participants. (B) Mean ASM resulting from the average across the C-surrogate avalanches (see Methods) computed based on the true avalanches shown in panel A. (C) Mean ASM of the true avalanches shown in panel A thresholded with the mean ASM of the C-surrogate avalanches shown in panel B (see Methods). (D, E) Mean ASM of the two avalanche clusters identified by the Louvain algorithm computed on the avalanches detected in the 10 participants. (F) Transient cross-regional coherence quantified by the $SGDC(\omega)$ measure (see Appendix A.3), associated with the two avalanche clusters shown in panels D and E. The $SGDC(\omega)$ measure was computed in a time-resolved manner around each detected avalanche by considering the time interval corresponding to the avalanche duration (see Methods). The small markers represent mean $|SGDC(\omega)|$ values averaged across the avalanches in each individual participant. The big markers represent mean $|SGDC(\omega)|$ values averaged across the 10 participants. (G) Same as in F for the synthetic data corresponding to the large-scale model. Symbols and abbreviations: ASM, Avalanche Spectral Matrix.

458 *Appendix B.3. Supplementary results excluding the deep sources*

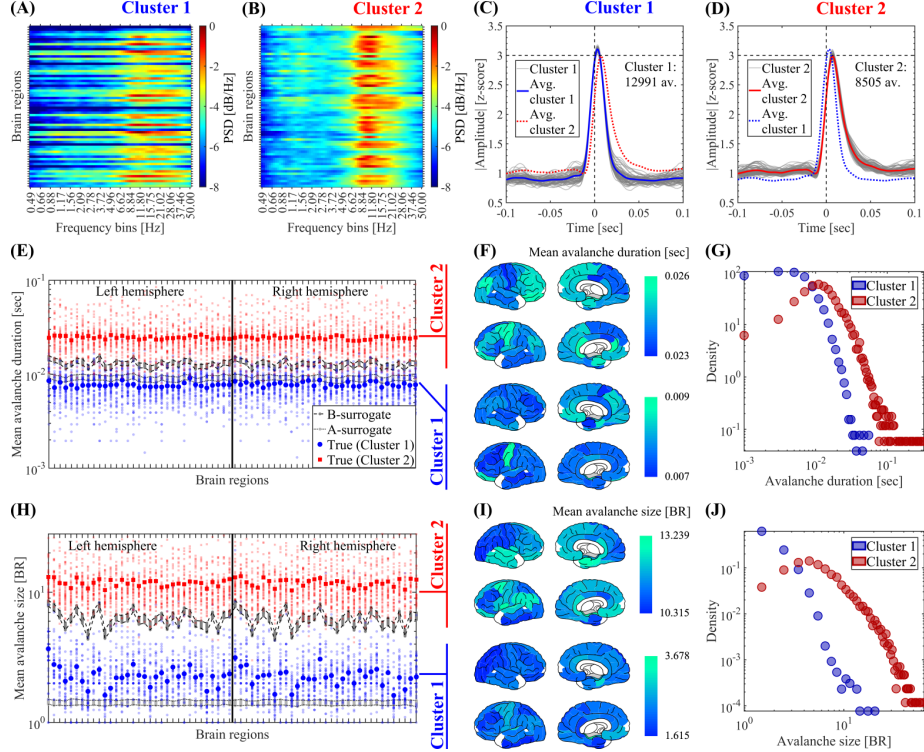


Figure B.11: Clustering of avalanches according to spectral signature. The avalanches obtained from 45 subjects were clustered using the Louvain algorithm (resolution parameter $\gamma = 1$, see Methods). (A, B) Mean ASM of the two avalanches clusters identified by the Louvain algorithm computed on the avalanches detected in the 45 participants. (C, D) Waveform shapes of the avalanches pertaining to the two avalanches clusters identified by the Louvain algorithm. Thin gray lines correspond to the average waveform shape in each brain region. Thick blue and red lines correspond to the resulting waveform shape averaged across the brain regions for avalanche cluster 1 and 2, respectively. (E) Spatial profile showing the mean duration of avalanches pertaining to cluster 1 (in blue) and cluster 2 (in red). For the true data, the small and big markers correspond to the mean spatial profile in each patient and the average across the 45 participants, respectively (see Methods). To test the significance of the difference of the mean avalanches duration between cluster 1 and cluster 2, in each brain region we computed a non-parametric permutation test (random sampling without replacement, 1×10^4 permutations). All the brain regions disclosed a statistically significant difference of the mean avalanches duration between cluster 1 and 2 (the Bonferroni-adjusted two-tailed P values result $P < 0.001$ in all the brain regions). (F) Brain topographies for the mean duration of neuronal avalanches averaged across the 45 participants as shown in panel E. (G) Distribution of the duration of avalanches pertaining to the cluster 1 and cluster 2 observed in the 45 participants. (H) Same as in E for the size of neuronal avalanches. To test the significance of the difference of the mean avalanches size between cluster 1 and cluster 2, in each brain region we computed a non-parametric permutation test (random sampling without replacement, 1×10^4 permutations). All the brain regions disclosed a statistically significant difference of the mean avalanches size between cluster 1 and 2 (the Bonferroni-adjusted two-tailed P values result $P < 0.001$ in all the brain regions). (I) Same as in F for the size of neuronal avalanches. (J) Same as in G for the size of neuronal avalanches. Symbols and abbreviations: BR, Brain Regions.

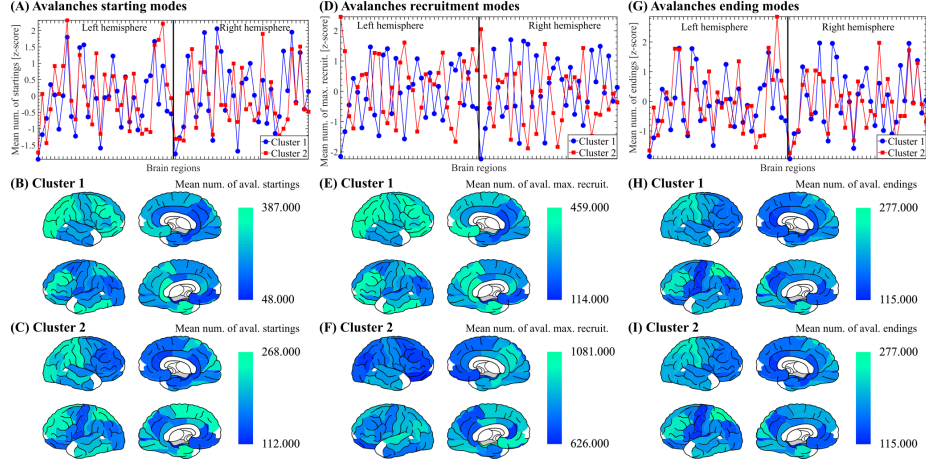


Figure B.12: Avalanche propagation modes. (A) Spatial profile for the avalanches starting modes corresponding to the two avalanche clusters (mean value across 41 participants). The avalanches obtained from 45 subjects were clustered using the Louvain algorithm (resolution parameter $\gamma = 1$, see Methods). The Pearson's correlation between the spatial profiles of cluster 1 and cluster 2 is $r = 0.584$, $P < 0.001$. (B) Brain topographies for the starting modes of cluster 1 avalanches as shown in panel A. (C) Brain topographies for the starting modes of cluster 2 avalanches as shown in panel A. (D-F) Same as A-B for avalanches maximum recruitment modes (see Methods). In panel D, the Pearson's correlation between the spatial profiles of cluster 1 and cluster 2 is $r = -0.842$, $P < 0.001$. (G-I) Same as A-B for avalanches ending modes (see Methods). In panel G, the Pearson's correlation between the spatial profiles of cluster 1 and cluster 2 is $r = 0.571$, $P < 0.001$. The reported P values for the statistical significance of the Pearson's correlation were assessed using Student's t distributions of the two-tailed hypothesis test under the null hypothesis that the correlation is zero.